PCH-2^{TRIP13} regulates spindle checkpoint strength

Lénaïg Défachelles, Anna E. Russo, Christian R. Nelson and Needhi Bhalla*

Department of Molecular, Cell and Developmental Biology, University of California, Santa Cruz,

Santa Cruz, CA 95064

*corresponding author: nbhalla@ucsc.edu

Department of Molecular, Cell and Developmental Biology

225 Sinsheimer Labs

University of California, Santa Cruz

Santa Cruz, CA 95064

phone: (831) 459-1319

fax: (831) 459-3139

Key words: *C. elegans*, mitosis, embryo, spindle assembly checkpoint, Mad2, aneuploidy, germline

ABSTRACT

Spindle checkpoint strength is dictated by three criteria: the number of unattached kinetochores, cell volume and cell fate. We show that the conserved AAA-ATPase, PCH-2/TRIP13, which remodels the checkpoint effector Mad2 from an active conformation to an inactive one, controls checkpoint strength in *C. elegans*. When we manipulate embryos to decrease cell volume, PCH-2 is no longer required for the spindle checkpoint or recruitment of Mad2 at unattached kinetochores. This role in checkpoint strength is not limited to large cells: the stronger checkpoint in germline precursor cells also depends on PCH-2. PCH-2 is enriched in germline precursor cells and this enrichment relies on conserved factors that induce asymmetry in the early embryo. Finally, the stronger checkpoint in germline precursor cells is regulated by CMT-1, the ortholog of $p31^{comet}$, which is required for both PCH-2's localization to unattached kinetochores and its enrichment in germline precursor cells. Thus, PCH-2, likely by regulating the availability of inactive Mad2 at and near unattached kinetochores, governs checkpoint strength. This role may be specifically relevant in scenarios where maintaining genomic stability is particularly challenging, such as in oocytes and early embryos enlarged for developmental competence and germline cells that maintain immortality.

INTRODUCTION

To prevent the missegregation of chromosomes and the production of daughter cells with an incorrect number of chromosomes, the spindle checkpoint (also called the spindle assembly checkpoint or the mitotic checkpoint) monitors whether chromosomes are attached to the spindle via kinetochores. If kinetochores fail to attach properly, this checkpoint delays the cell cycle to promote error correction and prevent aneuploidy. Despite its critical role, the duration of the cell cycle delay, defined as the strength of the spindle checkpoint, can be highly variable. This variability can be controlled by the number of unattached kinetochores (Collin *et al.*, 2013), cell volume (Galli and Morgan, 2016; Kyogoku and Kitajima, 2017), and cell fate (Galli and Morgan, 2016; Gerhold *et al.*, 2018).

The spindle checkpoint response initiates with the recruitment of Mad1 and Mad2 at unattached kinetochores (Chen *et al.*, 1996; Li and Benezra, 1996; Chen *et al.*, 1998; Sironi *et al.*, 2001), which catalyzes the production of a Mitotic Checkpoint Complex (MCC). The MCC enforces a checkpoint arrest by inhibiting the Anaphase Promoting Complex/Cyclosome (APC/C) and preventing cell cycle progression (Sudakin *et al.*, 2001). Formation of the MCC is driven by conformational changes in Mad2, which can exist in an open conformation (O-Mad2) or a closed conformation (C-Mad2) (Luo *et al.*, 2002; Sironi *et al.*, 2002; Luo *et al.*, 2004). Mad2 is in the closed conformation in the Mad1/Mad2 tetramer recruited to unattached kinetochores. C-Mad2 in the tetramer acts as a template to convert additional soluble O-Mad2 to C-Mad2, which can be assembled into the MCC (Sironi *et al.*, 2001; De Antoni *et al.*, 2005; Simonetta *et al.*, 2009; Fava *et al.*, 2011). Thus, unattached kinetochores act as a platform for MCC assembly. This soluble signal generated by unattached kinetochores effectively tunes the spindle

68 checkpoint response: the length of the cell cycle delay imposed by the checkpoint is
69 governed by the ratio of unattached kinetochores producing MCC, and its ability to inhibit
70 the APC, to cytoplasmic volume (Collin *et al.*, 2013; Dick and Gerlich, 2013; Galli and
71 Morgan, 2016; Kyogoku and Kitajima, 2017).
72
73 PCH-2/TRIP13 is a hexameric AAA+ ATPase that remodels HORMA domain-containing
74 proteins, a group that includes Mad2 (Aravind and Koonin, 1998; Rosenberg and
75 Corbett, 2015; Vader, 2015). Biochemical and structural studies have shown that PCH-2
76 converts C-Mad2 to O-Mad2 (Ye *et al.*, 2015; Brulotte *et al.*, 2017; Alfieri *et al.*, 2018).
77 TRIP13 works with the adaptor protein p31^{comet} to extract C-Mad2 from the MCC and
78 promote its disassembly, permitting the activation of the APC/C and silencing the
79 checkpoint (Eytan *et al.*, 2014; Wang *et al.*, 2014; Miniowitz-Shemtov *et al.*, 2015; Ye *et*
80 *al.*, 2015; Brulotte *et al.*, 2017; Alfieri *et al.*, 2018). In addition to this role, we and others
81 have shown that PCH-2/TRIP13 is essential for spindle checkpoint activation in *C.*
82 *elegans* and mammalian cells (Nelson *et al.*, 2015; Ma and Poon, 2016; Yost *et al.*,
83 2017; Ma and Poon, 2018). PCH-2 is present at unattached kinetochores (Tipton *et al.*,
84 2012; Wang *et al.*, 2014; Nelson *et al.*, 2015) and is required to robustly localize Mad2,
85 but not Mad1, to unattached kinetochores (Nelson *et al.*, 2015; Yost *et al.*, 2017). A
86 major implication of this work is that O-Mad2 can be limiting during checkpoint activation
87 and PCH-2/TRIP13 plays a central role in ensuring its availability (Ma and Poon, 2018).
88
89 Based on a genetic interaction between the *C. elegans* ortholog of p31^{comet}, CMT-1, and
90 PCH-2, we had previously proposed that PCH-2 disassembles a CMT-1/Mad2 complex
91 to promote checkpoint signaling, similar to its role during checkpoint silencing (Nelson *et*
92 *al.*, 2015). However, recent data from mammalian systems, in which loss of p31^{comet}
93 does not suppress the requirement for TRIP13 (Nelson *et al.*, 2015; Ma and Poon, 2016;

94 Yost *et al.*, 2017; Ma and Poon, 2018) and TRIP13's function becomes essential for
95 checkpoint activity only when O-Mad2 becomes limiting (Ma and Poon, 2018), suggest
96 an alternative model in *C. elegans*. In this model, some Mad2, likely C-Mad2, is
97 complexed with and stabilized by CMT-1, explaining the reduction in total Mad2 protein
98 levels in *cmt-1* mutants. Despite this reduction of Mad2, we propose that in the absence
99 of CMT-1, more O-Mad2 is available, thus making PCH-2 partially dispensable and
100 explaining the genetic suppression. This model differs from our understanding of TRIP13
101 and p31^{comet} in mammalian cells, potentially because relative levels of C and O-Mad2
102 may vary between systems and most Mad2 in mammalian cells is present as O-Mad2
103 (Luo *et al.*, 2004). Further, it highlights the importance of studying spindle checkpoint
104 function in developmentally-relevant model organisms.
105
106 This model, however, raises another question: if the primary role of PCH-2/TRIP13 is to
107 guarantee enough O-Mad2 is available for checkpoint activation and this role can be
108 dispensable when enough O-Mad2 is available, is there a reason for PCH-2/TRIP13 to
109 localize to unattached kinetochores (Tipton *et al.*, 2012; Wang *et al.*, 2014; Nelson *et al.*,
110 2015)? One possible answer comes from our additional analysis of *cmt-1* mutant worms.
111 In addition to its role as a PCH-2 adapter (Ye *et al.*, 2015) and stabilizing Mad2 protein
112 levels (Nelson *et al.*, 2015), CMT-1 is also required to localize PCH-2 to unattached
113 kinetochores during the spindle checkpoint response and generate a robust spindle
114 checkpoint response in AB cells (Nelson *et al.*, 2015). Overexpressing Mad2 does not
115 suppress the partial defect in spindle checkpoint activation in *cmt-1* mutants (Nelson *et*
116 *al.*, 2015), suggesting that the defect in spindle checkpoint strength is not because of
117 reduced Mad2 protein levels but the inability to localize PCH-2 to unattached
118 kinetochores.
119

120 Here, we test this possibility and show that PCH-2 controls spindle checkpoint strength
121 in *C. elegans*. Despite being essential for the spindle checkpoint in the large somatic, or
122 AB, cell of the 2-cell embryo (Nelson *et al.*, 2015), PCH-2 becomes dispensable for the
123 spindle checkpoint and partially dispensable for Mad2 recruitment at unattached
124 kinetochores as AB cells are genetically manipulated to become smaller. The
125 requirement for PCH-2 in promoting spindle checkpoint strength is also observed as
126 cells decrease in size during embryogenesis and in germline precursor, or P_1, cells,
127 which have a stronger checkpoint than their somatic counterparts. PCH-2 is enriched in
128 P_1 cells and this enrichment depends on conserved regulators of embryonic polarity,
129 PAR-1 and PAR-6. Further, the stronger checkpoint in P_1 cells also relies on the *C.*
130 *elegans* ortholog of $p31^{comet}$, CMT-1, indicating that CMT-1's ability to enrich PCH-2 in P_1
131 cells, in addition to its role in localizing PCH-2 to unattached kinetochores, contributes to
132 a stronger checkpoint. We propose that PCH-2, and its mammalian ortholog TRIP13,
133 ensure a robust spindle checkpoint response and proper chromosome segregation by
134 regulating the availability of O-Mad2 at and near unattached kinetochores. This role may
135 be specifically relevant in scenarios where maintaining genomic stability is particularly
136 challenging, such as in oocytes and early embryos enlarged for developmental
137 competence and germline cells that maintain immortality.
138
139 **RESULTS**
140
141 **PCH-2 becomes dispensable for the spindle checkpoint response in somatic cells**
142 **experimentally reduced in size**
143 In the large somatic, or AB, cell of the *C. elegans* 2-cell embryo, PCH-2 is essential for
144 spindle checkpoint activation (Nelson *et al.*, 2015). To further assess the requirements
145 for PCH-2 function, we manipulated the cell volume of embryos, and thus AB cells,

146 experimentally by performing RNA interference (RNAi) against *ani-2*. *ani-2* encodes a
147 germline specific anillin whose depletion generates oocytes and, after fertilization,
148 embryos, of varying size (Maddox *et al.*, 2005) (Figure 1A). We monitored the length of
149 mitosis in these AB cells, using the time between nuclear envelope breakdown (NEBD)
150 to the onset of cortical contractility (OCC) as markers for the entry into and exit from
151 mitosis, respectively (Essex *et al.*, 2009). We then correlated the length of mitosis to
152 cytoplasmic volume. RNAi of *ani-2* did not affect cell cycle progression in control, *pch-2*,
153 or *mad-1* mutants (Figure S1A), indicating that reducing cytoplasmic volume did not
154 affect mitotic timing in AB cells. (In *C. elegans*, the genes that encode Mad1 and Mad2
155 are *mdf-1* and *mdf-2*, respectively. To avoid confusion, we will use *mad-1* and *mad-2*).
156
157 We performed double depletion of *ani-2* and *zyg-1* to induce the spindle checkpoint
158 response in control embryos, *pch-2*, and *mad-1* mutants. ZYG-1 is essential for
159 centrosome duplication and after the first embryonic division, its depletion generates
160 monopolar spindles (O'Connell *et al.*, 2001) and unattached kinetochores (Essex *et al.*,
161 2009) (Figure 1B). Consistent with previous reports, as AB cells decreased in cell
162 volume the length of the cell cycle delay, an indicator of spindle checkpoint strength,
163 increased in control embryos (Galli and Morgan, 2016; Gerhold *et al.*, 2018) (Figure 1C,
164 Videos 1 and 2). Surprisingly, as *pch-2* mutants decreased in size, the spindle
165 checkpoint response more closely resembled that of control AB cells than *mad-1*
166 mutants (Figure 1C, Videos 3 and 4). *mad-1* mutant embryos appear more sensitive to
167 *ani-2* RNAi treatment and we had difficulty recovering any wild-type sized *mad-1*
168 embryos. There was no significant difference between the slopes of the regression
169 analysis of control and *pch-2* mutant data (p value = 0.4664), while the slopes between
170 the regression analysis of *pch-2* and *mad-1* mutant data were significantly different (p
171 value = 0.0007). To make these comparisons more clear, we binned our data. By our

172 measurements, control AB cells ranged from 5 to 6 x 10^3 μm^3. Therefore, we classified
173 AB cells which were more than 5 x 10^3 μm^3 as wildtype sized. The remaining cells, which
174 ranged from 1.5 x 10^3 μm^3 to 5 x 10^3 μm^3 were partitioned equally into two classes:
175 medium sized embryos were between 3.3 x 10^3 μm^3 and 5 x 10^3 μm^3 and small embryos
176 were between 1.5 x 10^3 μm^3 and 3.3 x 10^3 μm^3. When partitioned into these classes,
177 *pch-2* mutants produced no checkpoint response in wildtype-sized AB cells, as
178 previously reported (Nelson *et al.*, 2015), defects in checkpoint strength in medium-sized
179 AB cells and a robust checkpoint response in small AB cells (Figure 1D).
180
181 We verified that the mitotic delay observed in *pch-2* AB cells was a legitimate spindle
182 checkpoint response by monitoring mitotic timing after performing double depletion of
183 *ani-2* and *zyg-1* in *san-1* and *pch-2;san-1* mutant embryos. SAN-1 is the *C. elegans*
184 ortholog of the essential spindle checkpoint factor, Mad3 (Nystul *et al.*, 2003) (Figure
185 S1B). There was no significant difference between the slopes of the regression analysis
186 of *san-1* and *pch-2;san-1* data (p value = 0.8813) and the slopes of each model were not
187 statistically different than zero (Figure S1B). However, we observed a slight increase in
188 the length of the cell cycle as cells got smaller in *san-1* mutants, potentially reflecting
189 that the spindle checkpoint in *C. elegans* is composed of two independent branches
190 (Essex *et al.*, 2009). These data allow us to draw two important conclusions: 1) Since we
191 observe robust spindle checkpoint activation in *pch-2* mutant AB cells as they decrease
192 in size and mitotic timing is similar to what we observe in control cells, PCH-2 does not
193 appear to affect spindle checkpoint silencing in *C. elegans*; and 2) the requirement for
194 PCH-2 during spindle checkpoint activation is proportional to cell volume in AB cells with
195 monopolar spindles.
196

197 **MAD-2 recruitment is partially restored to unattached kinetochores in *pch-2***
198 **somatic cells experimentally reduced in size**
199 We showed that PCH-2 is required for robust recruitment of Mad2 at unattached
200 kinetochores during spindle checkpoint activation in AB cells of 2-cell embryos (Nelson
201 *et al.*, 2015). Therefore, we tested whether the checkpoint induced delay we observed in
202 small *ani-2*^{RNAi}*;zyg-1*^{RNAi}*;pch-2* AB cells was accompanied by increased recruitment of
203 GFP::MAD-2 at unattached kinetochores. We quantified GFP::MAD-2 recruitment at
204 unattached kinetochores in pseudo-metaphase in control animals and *pch-2* mutants
205 treated with *ani-2* and *zyg-1* RNAi (Figure 2A) and plotted GFP::MAD-2 fluorescence
206 against cell volume (Figure 2B). Surprisingly, the regression analysis for control AB cells
207 had a positive slope, suggesting that less GFP::MAD-2 is required at unattached
208 kinetochores for spindle checkpoint function as these cells became smaller (Figure 2B).
209 This was despite similar levels of soluble GFP::MAD2 around mitotic chromosomes after
210 NEBD in both genetic backgrounds (Figures S2A and S2B). We observed that the
211 regression analysis of GFP::MAD-2 fluorescence at unattached kinetochores in *pch-*
212 *2;ani-2*^{RNAi}*;zyg-1*^{RNAi} AB cells exhibited a negative slope, showing improved GFP::MAD-2
213 recruitment to unattached kinetochores as cells got smaller. However, the amount of
214 GFP::MAD-2 was typically lower in fluorescence intensity than *ani-2*^{RNAi}*;zyg-1*^{RNAi} control
215 cells (Figure 2B). Therefore, our experiments demonstrate that MAD-2 recruitment is
216 partially restored to unattached kinetochores in *pch-2* mutant somatic cells
217 experimentally reduced in size.
218
219 **MAD-2 dosage controls checkpoint strength**
220 *C. elegans* meiotic nuclei in the germline exist in a syncytium and cellularize after
221 completing meiotic prophase. Knockdown of *ani-2* affects this cellularization event,
222 resulting in a loss of cytoplasmic volume after nuclei are fully formed (Maddox *et al.*,

223 2005). MAD-2 is localized to the nucleus and nuclear envelope in these oocytes (Bohr *et*
224 *al.*, 2015; Lawrence *et al.*, 2015) (Figure 3A). Since embryonic nuclear size is not
225 affected by *ani-2* RNAi (Figure S3), we reasoned that as cells are genetically
226 manipulated to decrease in cell volume, the absolute amount of Mad2 protein is likely to
227 remain constant but its concentration increases. Given that TRIP13 function is
228 dispensable for checkpoint activation when O-Mad2 is readily available in mammalian
229 cells (Ma and Poon, 2018), we reasoned that something similar might be happening in
230 *C. elegans* embryos. Specifically, we hypothesized that an increase in concentration of
231 Mad2, and O-Mad2 in particular, may explain the reduced requirement for PCH-2 in *ani-*
232 2^{RNAi};$zyg\text{-}1^{RNAi}$ small AB cells (Figure 3B).
233
234 To test this possibility, we initially attempted to directly visualize O-Mad2 in *C. elegans*
235 embryos. Unfortunately, we were unable to perform this experiment with a commercial
236 antibody (data not shown). Further, we could not directly probe total Mad2 concentration
237 as cells decrease in volume upon treatment with *ani-2* RNAi because GFP::MAD-2 does
238 not localize to the nucleus and instead localizes in the cytoplasm until NEBD (Essex *et*
239 *al.*, 2009; Nelson *et al.*, 2015), making it an inaccurate reporter for this assay. Instead,
240 we tested whether reducing Mad2 dosage affected checkpoint strength. We
241 hypothesized that if Mad2 concentration influences checkpoint strength, reducing it by
242 half should attenuate checkpoint strength in comparison to control animals. We
243 performed double depletion of *ani-2* and *zyg-1* by RNAi in *mad-2* heterozygotes. Indeed,
244 *mad-2* heterozygotes exhibited stronger spindle checkpoint strength as cells became
245 smaller. However, the increase in spindle checkpoint strength was less robust than
246 control cells (Figure 3C). The slopes of the linear regressions for both control and *mad-2*
247 heterozygotes were significantly non-zero, unlike similar experiments with *mad-1* and

248 *san-1* homozygotes (Figures 1B and S1D). Therefore, spindle checkpoint strength
249 depends on MAD-2 dosage.
250
251 We wondered whether the decrease in Mad2 protein levels might restore the reliance on
252 PCH-2 in small embryos. However, *pch-2;mad-2/*+ double mutants exhibited a
253 substantial decrease in the production and viability of embryos, preventing us from
254 performing these experiments: *pch-2;mad-2/*+ double mutants produced broods that
255 were 14% of control animals and only 1% of these embryos were viable. Further, *pch-*
256 *2;mad-2* double mutants could not be recovered from *pch-2;mad-2/*+ mothers, a genetic
257 interaction that we did not observe when we generated *pch-2;mad-1* double mutants
258 (Bohr *et al.*, 2015) or *pch-2;san-1* double mutants (Figure S1B). Worms with mutations in
259 some spindle checkpoint mutants often display defects in fertility, viability and
260 development (Kitagawa and Rose, 1999; Stein *et al.*, 2007; Lara-Gonzalez *et al.*, 2019).
261 Thus, in addition to MAD-2 dosage controlling checkpoint strength, it collaborates with
262 PCH-2 to promote *C. elegans* fertility and viability.
263
264 **PCH-2 affects spindle checkpoint strength during embryogenesis**
265 During embryogenesis, cell volume decreases and spindle checkpoint strength
266 increases (Galli and Morgan, 2016; Gerhold *et al.*, 2018). Given that the requirement for
267 PCH-2 is proportional to cell volume in 2-cell embryos treated with *ani-2* RNAi, we
268 assessed the role for PCH-2 in spindle checkpoint activation as cells decreased in size
269 during normal embryogenesis.
270
271 We permeabilized embryos by performing *perm-1* RNAi (Carvalho *et al.*, 2011) and
272 activated the spindle checkpoint by treating these *perm-1*^{RNAi} embryos with nocodazole,
273 a drug that depolymerizes microtubules. Since we could not reliably visualize OCC in

274 these dividing embryos, we measured mitotic timing from nuclear envelope break down
275 (NEBD) to decondensation of chromosomes (DECON) in cells of the AB lineage. These
276 cells in control embryos exhibited a longer mitotic delay in 16-cell than in 4-cell embryos
277 (Figure 4A), verifying that the spindle checkpoint increases in strength as cells decrease
278 in volume during embryogenesis (Galli and Morgan, 2016; Gerhold *et al.*, 2018). As a
279 control, we performed the same experiment in *san-1* mutants and did not detect a mitotic
280 delay when these embryos were treated with nocodazole (Figure 4A). Cells in 4-cell *pch-*
281 *2* mutant embryos treated with nocodazole resembled *san-1* mutants (Figure 4A).
282 However, cells in the AB lineage in 16-cell *pch-2* mutant embryos treated with
283 nocodazole exhibited a significant cell cycle delay when compared to similar cells in *pch-*
284 *2* mutants treated with DMSO and *san-1* mutants treated with nocodazole. These delays
285 were not as prolonged as that observed in control embryos treated with nocodazole
286 (Figure 4A). Thus, as cells of the AB lineage naturally decrease in cell size to 16 cell
287 embryos, *pch-2* mutants treated with nocodazole delay the cell cycle but exhibit defects
288 in spindle checkpoint strength.
289
290 Given our hypothesis that Mad2 dosage might contribute to spindle checkpoint strength,
291 particularly in *pch-2* mutants, we tested if a subtle increase in MAD-2 protein levels
292 would suppress the defect in spindle checkpoint function or strength in *pch-2* mutant
293 embryos. The presence of a GFP::MAD-2 transgene, in addition to endogenous MAD-2,
294 results in about 2.5 times more MAD-2 in worms. This slight overexpression generates a
295 normal spindle checkpoint response in control AB cells and can bypass the requirement
296 for checkpoint components MAD-3 or BUB-3 (Essex et al., 2009), but not PCH-2 (Nelson
297 et al., 2015) in AB cells of 2-cell embryos with monopolar spindles. Overexpression of
298 MAD-2 did not affect the checkpoint response in 16-cell *pch-2* embryos (Figure 4B).
299 However, in contrast to our results in 4-cell *pch-2* mutant embryos treated with

300 nocodazole (Figure 4A), we found that overexpression of MAD-2 in cells of the AB
301 lineage of 4-cell *pch-2* embryos produced cell cycle delays when compared to the same
302 cells in embryos treated with DMSO. Again, these delays were not as dramatic as
303 control cells overexpressing GFP::MAD-2 (Figure 4B) but were significant, allowing us to
304 conclude that slight overexpression of Mad2 partially restores checkpoint function to
305 *pch-2* mutants as cells of the AB lineage decrease in size during embryogenesis, at least
306 in 4-cell embryos.
307
308 Given that we activated the spindle checkpoint in *ani-2*^{RNAi} embryos by generating
309 monopolar spindles (Figures 1C and 3C), we also tested whether embryos with
310 monopolar spindles might behave differently than embryos treated with nocodazole,
311 particularly in very early embryogenesis. We used a fast acting temperature sensitive
312 allele of *zyg-1* (*zyg-1*^{ts}) (O'Rourke *et al.*, 2011) to activate the spindle checkpoint in
313 developing embryos with 2, 4 and 8 cells. We shifted embryos at different stages of
314 development, verified the appearance of monopolar spindles and measured mitotic
315 timing from NEBD to DECON. In control *zyg-1*^{ts} mutant embryos, we observed a delay in
316 mitotic timing in cells from the AB lineage and this delay only became marginally longer
317 as embryos had more cells (Figure 4C), similar to previous reports (Gerhold *et al.*,
318 2018). In stark contrast to our *ani-2*^{RNAi} experiments, the mitotic timing observed in *pch-*
319 *2;zyg-1*^{ts} mutant embryos was the same in AB cells of 2-cell, 4-cell and 8-cell embryos
320 and significantly reduced in comparison to *zyg-1*^{ts} embryos. Thus, similar to our results
321 with 4-cell *pch-2* mutant embryos treated with nocodazole, *pch-2* mutants exhibit no cell
322 cycle delay in the presence of monopolar spindles in AB cells in 2-cell, 4-cell and 8-cell
323 embryos. However, additional considerations may make direct comparisons between our
324 *ani-2*^{RNAi}*;zyg-1*^{RNAi} experiments and *zyg-1*^{ts} embryos difficult (see Discussion).
325

326 **PCH-2 is responsible for the stronger spindle checkpoint in the germline lineage**

327 Cell fate is another important determinant of spindle checkpoint strength. In *C. elegans*
328 embryos, the spindle checkpoint is stronger in germline precursor cells than similarly
329 sized somatic counterparts (Galli and Morgan, 2016; Gerhold *et al.*, 2018). However, as
330 we observed with AB cells (Nelson *et al.*, 2015), PCH-2 is essential for the spindle
331 checkpoint in wildtype-sized P_1 cells (Figure S4). Therefore, having established that
332 PCH-2 becomes dispensable for the spindle checkpoint as 2-cell embryos are
333 genetically manipulated to become smaller (Figures 1C and D), we tested whether PCH-
334 2 contributed to the stronger spindle checkpoint in P_1 cells of 2-cell embryos treated with
335 *ani-2* RNAi (Figures 5 and S4B). Consistent with other reports (Galli and Morgan, 2016;
336 Gerhold *et al.*, 2018), when we performed double depletion of *ani-2* and *zyg-1* in control
337 embryos and monitored mitotic timing, we observed P_1 cells with similar volumes as AB
338 cells exhibiting a longer cell cycle delay (Figures 5A and S4B, Videos 5 and 6). Further,
339 the regression analysis that best fit control P_1 data is significantly different and steeper
340 than that of control AB cells (p value < 0.0001), indicating that variables in addition to
341 cell volume contribute to the spindle checkpoint strength in germline precursor cells.
342 When we knocked down both *ani-2* and *zyg-1* in *pch-2* mutant embryos, we no longer
343 observed a significant difference (p value = 0.9096) between the slopes of the
344 regression analysis of P_1 and AB cells (Figures 5B and S4B, Videos 7 and 8), indicating
345 that PCH-2 is responsible for the stronger checkpoint in P_1 cells.

346

347 We observed that cell cycle timing was faster in *pch-2* mutant P_1 cells than similarly
348 sized *pch-2* mutant AB cells after treatment with *ani-2* and *zyg-1* RNAi (Figures 5B and
349 S4B). We wondered if embryonic germline precursor cells might rely on some spindle
350 checkpoint proteins for normal mitotic timing, analogous to mitotically dividing stem cells
351 in the *C. elegans* germline (Gerhold *et al.*, 2015) and similar to mammalian cultured cells

352 (Meraldi *et al.*, 2004; Rodriguez-Bravo *et al.*, 2014; Ma and Poon, 2016). To address
353 this, we measured normal mitotic timing in AB and P_1 cells of both control and *pch-*
354 *2* mutant embryos. We found that while normal mitotic timing is unaffected by mutation of
355 *pch-2* in AB cells, *pch-2* mutant P_1 cells go through mitosis significantly faster than
356 control P_1 cells (Figure 5C), thus providing an explanation for the faster cell cycle timing
357 in *pch-2* mutant P_1 cells with the same cell volume as *pch-2* mutant AB cells after
358 treatment with *ani-2* and *zyg-1* RNAi. We saw a decrease in the cell cycle timing of P_1
359 cells in *mad-1* mutants but this was not significantly different than control P_1 cells (Figure
360 5C).
361
362 **PCH-2's enrichment in P_1 cells depends on PAR-1 and PAR-6**
363 Cell fate is driven by the asymmetric distribution of various determinants between
364 somatic and germline lineages during early divisions of the *C. elegans* embryo (Rose
365 and Gonczy, 2014). Since we found that PCH-2 promoted the spindle checkpoint
366 strength in both AB and P_1 cells, but even more dramatically in P_1 cells, we asked if
367 PCH-2 was regulated differently between these cells. First, we tested whether PCH-
368 2::GFP could also support the stronger checkpoint in P_1 cells. We treated embryos
369 expressing PCH-2::GFP with *zyg-1* RNAi and evaluated mitotic timing in both AB and P_1
370 cells, in control cells and in the presence of monopolar spindles, using chromosome
371 decondensation as a marker for mitotic exit. P_1 cells expressing PCH-2::GFP had full
372 checkpoint function, exhibiting a mitotic delay longer than AB cells also expressing PCH-
373 2::GFP (Figure 6A).
374
375 Previous transcriptome analysis of PCH-2 did not reveal asymmetric enrichment of PCH-
376 2 mRNA between AB and P_1 cells (Tintori *et al.*, 2016). We tested whether PCH-2::GFP

377 exhibited differences in protein levels between AB and P_1 cells. First, we assessed
378 whether PCH-2::GFP was more enriched in pseudo-metaphase at unattached
379 kinetochores in P_1 than AB cells. We quantified PCH-2::GFP fluorescence at unattached
380 kinetochores in both AB and P_1 cells of embryos treated with *zyg-1* RNAi but did not
381 detect any difference between the two cell types (Figures S5A and B). Similarly, we did
382 not detect any difference in GFP::MAD-2 recruitment at unattached kinetochores
383 between AB and P_1 cells in *zyg-1*^{RNAi} embryos (Figures S5C and D).
384
385 Checkpoint factors, including MAD-2 and PCH-2, form a diffuse "cloud" around mitotic
386 chromosomes after NEBD, even during normal cell cycles (Essex *et al.*, 2009; Nelson *et*
387 *al.*, 2015). We wondered if PCH-2::GFP fluorescence in this cloud might be different
388 between AB and P_1 cells. First, we verified that PCH-2::GFP fluorescence around mitotic
389 chromosomes was similar between AB cells during unperturbed (control) or monopolar
390 mitosis (*zyg-1*^{RNAi}) (Figure S6). PCH-2::GFP fluorescence around chromosomes was
391 significantly higher in *zyg-1*^{RNAi} AB cells than control AB cells (Figure S6B). However, we
392 noticed that the area occupied by PCH-2::GFP in control AB cells was significantly larger
393 than that of *zyg-1*^{RNAi} AB cells (yellow dashed circle in Figure S6A and quantified in
394 Figure S6C). When we factored this larger area of PCH-2::GFP fluorescence into our
395 analysis, we observed a similar amount of PCH-2::GFP around mitotic chromosomes in
396 both control and *zyg-1*^{RNAi} AB cells (Figure S6D).
397
398 Having established that AB cells had similar amounts of PCH-2::GFP whether the
399 checkpoint was active or not, we quantified PCH-2::GFP fluorescence in the area around
400 mitotic chromosomes in AB and P_1 cells during unperturbed cell cycles. Similar to AB
401 cells (Nelson *et al.*, 2015) and Figure S6A), we observed PCH-2::GFP enriched in the
402 area around the chromosomes in prometaphase in P_1 cells (Figure 6B). When we

403 quantified the fluorescence of PCH-2::GFP in this area surrounding chromosomes after
404 NEBD in both AB and P_1 cells, we detected a statistically significant enrichment of PCH-
405 2::GFP in the area surrounding chromosomes in P_1 cells (Figure 6C) but not in the
406 cytoplasm of P_1 cells (Figures S7A and B). Although this enrichment is limited to a
407 "cloud" around mitotic chromosomes (see Figure S7B), we verified that this enrichment
408 was not the indirect consequence of the smaller volume of P_1 cells by quantifying PCH-
409 2::GFP fluorescence in *gpr-1/2*^{RNAi} embryos. This double knockdown equalizes the size
410 of AB and P_1 cells without affecting their cell fate (Colombo *et al.*, 2003; Gotta *et al.*,
411 2003; Srinivasan *et al.*, 2003). RNAi of *gpr-1/2* showed variability in the effect on AB and
412 P_1 cell size (Figure S7C). However, when we limited our analysis of PCH-2::GFP
413 fluorescence to embryos in which AB and P_1 cells were of similar area (red symbols in
414 Figure S7C), we observed a similar enrichment of PCH-2::GFP in P_1 cells as control
415 embryos (Figures S7D and E).
416
417 To better understand the relationship between PCH-2 enrichment in P_1 cells and cell
418 fate, we abrogated the asymmetry of the 2-cell embryo by performing RNAi against the
419 essential polarity factors, PAR-1 (Guo and Kemphues, 1995) and PAR-6 (Hung and
420 Kemphues, 1999). These factors antagonize each other, with PAR-6 at the anterior
421 cortex and PAR-1 at the posterior cortex of early embryos, to establish asymmetries
422 during the first two embryonic divisions (Goldstein and Macara, 2007). In both *par-1*^{RNAi}
423 and *par-6*^{RNAi} mutant embryos, AB and P_1 cells exhibit similar checkpoint strength
424 (Gerhold *et al.*, 2018), indicating that the stronger spindle checkpoint response in P_1
425 cells depends on this asymmetric division. Despite the loss of cell fate in *par-1*^{RNAi} and
426 *par-6*^{RNAi} embryos, we will refer to the anterior blastomere as "AB" and the posterior as
427 "P_1". We verified the efficiency of *par-1* and *par-6* RNAi by measuring cell area and
428 found that AB and P_1 cells approached similar sizes in both conditions (Figures S8A and

429 B), although AB cells were still significantly larger than P_1 cells in *par-1*^{RNAi} mutant
430 embryos (Figure S8A). We quantified PCH-2::GFP fluorescence in the area around
431 chromosomes in AB and P_1 cells after *par-1* RNAi and observed that the fluorescence of
432 PCH-2::GFP, despite being slightly lower in P_1 cells, was not significantly different
433 between AB and P_1 cells, unlike what we observed in embryos exposed to control RNAi
434 (Figures 6D and E). AB and P_1 cells treated with *par-6* RNAi showed equal PCH-2::GFP
435 fluorescence (Figures S8C and D). Therefore, PCH-2::GFP's enrichment around mitotic
436 chromosomes in P_1 cells depends on the conserved factors that induce embryonic
437 asymmetry and germline cell fate, PAR-1 and PAR-6.
438
439 **The stronger checkpoint in P_1 cells depends on CMT-1**
440 In vitro, the *C. elegans* ortholog of p31^{comet}, CMT-1, is required for PCH-2 to bind and
441 remodel Mad2 (Ye *et al.*, 2015). In addition to this role, CMT-1 is also required to localize
442 PCH-2 to unattached kinetochores and generate a robust spindle checkpoint response
443 in AB cells (Nelson *et al.*, 2015). Therefore, we reasoned that CMT-1 might also be
444 required for the stronger checkpoint in P_1 cells.
445
446 To test this possibility, we first performed double knockdown of *ani-2* and *zyg-1* in *cmt-1*
447 mutants and monitored the length of the spindle checkpoint response as AB and P_1 cells
448 became smaller (Figure 7A, Videos 9-12). When compared to the regression model for
449 control AB cells (opaque blue line in Figure 7A), we saw that *cmt-1* AB cells consistently
450 exhibit a weaker checkpoint at all cell volumes. Similar to *pch-2;ani-2*^{RNAi}*;zyg-1*^{RNAi}
451 mutants (Figure 5B), the stronger spindle checkpoint response in P_1 cells was lost in
452 *cmt-1;ani-2*^{RNAi}*;zyg-1*^{RNAi} mutants and we did not observe any statistical difference
453 between the between the slopes of the regression analysis of P_1 and AB cells (p value =
454 0.9403). We also observed that cell cycle timing was faster in *cmt-1* P_1 cells that were

455 similar in volume to *cmt-1* AB cells (Figure 7A). Thus, CMT-1 is also essential to
456 promote spindle checkpoint strength in germline precursor cells.
457

458 We also performed *zyg-1* RNAi on control and *cmt-1* mutant embryos and monitored
459 mitotic timing in both AB and P_1 cells. AB and P_1 cells of control and *cmt-1* mutant
460 embryos treated with control RNAi had similar mitotic timing. Unlike similar experiments
461 in *pch-2* mutants (Figure 5C), we did not detect a statistically significant difference
462 between cell cycle time in P_1 cells between wildtype and *cmt-1* mutants embryos (Figure
463 7B), suggesting that *ani-2*^{RNAi}*;zyg-1*^{RNAi} embryos might be more sensitive to subtle
464 perturbations in cell cycle timing. In *zyg-1*^{RNAi} embryos, P_1 cells exhibited a stronger
465 checkpoint response than AB cells (Figure 7B). By contrast, both AB and P_1 cells in *cmt-*
466 *1*;*zyg-1*^{RNAi} mutant embryos exhibited similar spindle checkpoint delays (Figure 7B).
467 Despite having spindle checkpoint responses that were less robust than that of control
468 *zyg-1*^{RNAi} embryos, AB and P_1 cells in *cmt-1* mutant embryos treated with *zyg-1* RNAi
469 spent significantly longer in mitosis than *cmt-1* mutant embryos treated with control RNAi
470 (Figure 7B), indicating that they activated a weaker spindle checkpoint response, similar
471 to our published results (Nelson *et al.*, 2015). More importantly, *cmt-1*;*zyg-1*^{RNAi} mutant
472 embryos failed to generate a stronger checkpoint in P_1 cells, consistent with *cmt-1;ani-*
473 *2*^{RNAi}*;zyg-1*^{RNAi} experiments (Figure 7A).
474

475 Aside from localizing PCH-2 to unattached kinetochores (Nelson *et al.*, 2015), we
476 wondered if CMT-1 was required for any other aspects of PCH-2 regulation. Therefore,
477 we tested whether CMT-1 was necessary for PCH-2's asymmetric enrichment in P_1
478 cells. We quantified PCH-2::GFP fluorescence in prometaphase in the area around
479 chromosomes in both *cmt-1* mutant AB and P_1 cells (Figure 7C). First, we found that

480 PCH-2::GFP fluorescence was slightly higher in AB cells in *cmt-1* mutants than control
481 embryos (Figure 7D). We saw a similar result in our *par-1* RNAi experiments, although in
482 both cases these increases were not statistically significant. However, unlike *par-1*^{RNAi}
483 embryos (Gerhold *et al.*, 2018), this increase in PCH-2::GFP was not accompanied by
484 an increase in checkpoint strength (Figure 7B), consistent with our hypothesis that the
485 weaker checkpoint in *cmt-1* AB cells is a consequence of PCH-2's absence from
486 unattached kinetochores (Nelson *et al.*, 2015). Further, when we compared the
487 quantification of PCH-2::GFP fluorescence in *cmt-1* mutant AB and P_1 cells (Figure 7C),
488 we did not detect a significant difference between the two cells (Figure 7D), unlike our
489 experiment in control embryos (Figures 6B and C), indicating that CMT-1 contributes to
490 the asymmetric enrichment of PCH-2 in P_1 cells. Thus, CMT-1 promotes spindle
491 checkpoint strength through two mechanisms: localizing PCH-2 to unattached
492 kinetochores and ensuring its enrichment in germline precursor cells.
493
494 **DISCUSSION**
495
496 The role of PCH-2, and its mammalian ortholog TRIP13, in the spindle checkpoint has
497 been enigmatic. Originally identified as a checkpoint silencing factor (Eytan *et al.*, 2014;
498 Wang *et al.*, 2014; Miniowitz-Shemtov *et al.*, 2015; Ye *et al.*, 2015; Brulotte *et al.*, 2017;
499 Alfieri *et al.*, 2018), more recent evidence also indicates a role in promoting the
500 checkpoint response (Nelson *et al.*, 2015; Ma and Poon, 2016; Yost *et al.*, 2017; Ma and
501 Poon, 2018). It's clear that the reliance on PCH-2/TRIP13 in checkpoint activation
502 reflects the relative levels and availability of O-Mad2 (Ma and Poon, 2018). We show
503 here that PCH-2 also controls checkpoint strength. Surprisingly, we can uncouple PCH-
504 2's requirement for checkpoint activation, which we detect in both AB and P_1 cells of
505 wildtype sized 2-cell embryos (Nelson *et al.*, 2015 and Figure S4), from the requirement

506 for spindle checkpoint strength, which we observe when we genetically manipulate cell
507 size of 2-cell embryos by *ani-2* RNAi (Figures 1C and 5B). Based on this, we propose
508 that PCH-2 regulates checkpoint strength not only by regulating O-Mad2 availability, but
509 by doing so specifically at and near unattached kinetochores, providing an unanticipated
510 mechanism to explain this phenomenon (Figure 8). This role in checkpoint strength
511 appears to be particularly important in large cells, such as oocytes and cells in early
512 embryos, as well as cells that give rise to immortal germ cells.
513
514 Our model assumes that 2-cell embryos have a significant amount of O-Mad2 available,
515 even when PCH-2 function is lost (Figure 8), unlike what is reported in mammalian cells
516 (Ma and Poon, 2016). Given that this is a developmental system in which embryos have
517 only undergone a single mitotic division before we perform our assays, we propose that
518 O-Mad2 is not limiting in very early embryos, even in *pch-2* null mutants. In this way, *C.*
519 *elegans* 2-cell embryos would be analogous to mammalian cells undergoing cell division
520 soon after acute depletion of TRIP13 (Ma and Poon, 2018). Unfortunately, we were
521 unable to directly probe O-Mad2 concentration or its availability at or near unattached
522 kinetochores in small *ani-2*^{RNAi} embryos or germline precursor cells. However, we think
523 that several pieces of data support our model (Figure 8). PCH-2's characterized
524 biochemical activity regulates the availability of O-Mad2 (Ye *et al.*, 2015; Brulotte *et al.*,
525 2017; Alfieri *et al.*, 2018), making this the likely mechanism through which PCH-2
526 regulates checkpoint strength. PCH-2 at unattached kinetochores in AB and P_1 cells
527 (Nelson *et al.*, 2015 and Figure 7B) and its enrichment around mitotic chromosomes in
528 P_1 cells (Figures 5A and 6C) correlates with a stronger checkpoint. The loss of PCH-2 or
529 this enrichment produces similar checkpoint strength between AB and P_1 cells (Gerhold
530 et al., 2018 and Figures 1C, 5B, 6E, S7D, 7A and 7D). Indeed, the equalization of PCH-
531 2::GFP between AB and P_1 cells that we observe in *par-1*^{RNAi} and *par-6*^{RNAi} embryos

532 (Figures 6E and S8D) is entirely consistent with the observation that in these mutants,
533 AB cells more closely resemble P_1 cells in spindle checkpoint strength (Gerhold et al.,
534 2018). Finally, checkpoint strength depends on Mad2 dosage (Figure 2C), particularly in
535 AB cells of 4-cell *pch-2* mutant embryos (Figure 4B).
536
537 Another prediction of our model is that overexpression of Mad2 should also make PCH-2
538 dispensable for spindle checkpoint activation. We've shown that subtle elevations of
539 Mad2 protein levels introduce a cell cycle delay in AB cells of 4-cell embryos treated with
540 nocodazole but not those treated with DMSO (Figure 4B), entirely consistent with our
541 model. However, it's not clear why we do not observe a similar effect in cells of the AB
542 lineage of 8-cell or 16-cell embryos that overexpress Mad2 (Figure 4B). Unfortunately,
543 more dramatic overexpression experiments are technically difficult in *C. elegans*.
544 Further, it's likely that strong overexpression of Mad2 in *C. elegans* embryos will delay
545 normal mitosis, consistent with similar findings in mammalian cells (Marks *et al.*, 2017)
546 and budding yeast (Mariani *et al.*, 2012). In this way, PCH-2's function may provide a
547 useful buffer: Since Mad2 protein levels may need to stay within a narrow range to allow
548 normal mitotic timing, PCH-2's localization at and near unattached kinetochores provide
549 a mechanism to increase O-Mad2's local concentration to promote effective and efficient
550 signaling during checkpoint activation.
551
552 The requirement for PCH-2 in spindle checkpoint strength is also seen as AB cells
553 normally decrease in volume during embryogenesis (Figure 4A), although not as
554 dramatically as when we genetically manipulate cell size (Figure 1C). The inconsistency
555 between our *ani-2* and embryogenesis experiments could be explained by a variety of
556 factors. O-Mad2 may eventually become limiting in cells of the AB lineage with
557 successive divisions after the 2-cell stage, resulting in a greater reliance on PCH-2

558 function. Moreover, it may also suggest that relative levels of O-Mad2 and C-Mad2 are
559 more stringently regulated as embryonic development progresses and the multi-cellular
560 embryo becomes more complex. This possibility is supported by our finding that PCH-2
561 regulates normal cell cycle timing in P_1 cells, but not AB cells (Figure 5C), which implies
562 that variations in O-Mad2/C-Mad2 ratios influence normal mitotic timing in cells with
563 specific developmental fates. In addition, unlike the nuclei of 2-cell embryos treated with
564 *ani-2*^{RNAi} (Figure S3), nuclear volume scales with cell volume during embryogenesis
565 (Gerhold *et al.*, 2018). Therefore, the concentration of Mad2 may not necessarily
566 increase as cell size decreases in cells of the developing embryo, making direct
567 comparisons between small cells obtained by *ani-2*^{RNAi} treatment and small cells
568 resulting from normal embryogenesis challenging. Finally, recent reports have indicated
569 that, during embryogenesis in other systems, cell volume may not be a major contributor
570 to spindle checkpoint strength (Chenevert *et al.*, 2019; Vazquez-Diez *et al.*, 2019).
571 Indeed, in *C. elegans*, when only AB cells are monitored during very early
572 embryogenesis (the 2-8 cell stage), they exhibit very minor increases, if any, in
573 checkpoint strength (Galli and Morgan, 2016; Gerhold *et al.*, 2018 and Figure 4). This
574 may suggest that cell fate is generally a more important determinant of spindle
575 checkpoint strength during normal embryogenesis, potentially reconciling reports from a
576 wide array of systems.
577
578 Our experiments identify CMT-1, the *C. elegans* ortholog of mammalian p31^{comet}, as an
579 important regulator of PCH-2 function and, as a result, checkpoint strength. In addition to
580 its requirement in facilitating PCH-2's ability to interact with its substrate, Mad2
581 (Miniowitz-Shemtov *et al.*, 2015; Ye *et al.*, 2015; Brulotte *et al.*, 2017; Alfieri *et al.*, 2018),
582 CMT-1 localizes PCH-2 to unattached kinetochores (Nelson *et al.*, 2015) and promotes
583 PCH-2's enrichment in P_1 cells (Figure 7D). We propose that both of these roles

584 contribute to checkpoint strength. In large AB cells, CMT-1 ensures PCH-2's presence at
585 unattached kinetochores, increasing the local concentration of O-Mad2, driving the
586 production of soluble C-Mad2 and MCC and enforcing a robust checkpoint (Figure 8A).
587 In P_1 cells, the combination of PCH-2's localization at kinetochores and its enrichment
588 around chromosomes and near unattached kinetochores produces a checkpoint
589 stronger than somatic cells (Figure 8C). It's striking that, when CMT-1 is absent, AB
590 cells, in which there is more PCH-2 (Figure 7D), and P_1 cells, which are slightly smaller
591 than AB cells, exhibit similar checkpoint strength (Figure 7B). This indicates that even
592 these cells depend on PCH-2 to be present at unattached kinetochores to increase the
593 local concentration of O-Mad2 and promote checkpoint strength.
594
595 P_1 cells in both *pch-2;ani-2*^{RNAi}*;zyg-1*^{RNAi} and *cmt-1;ani-2*^{RNAi}*;zyg-1*^{RNAi} mutants show
596 faster cell cycle timing than similarly sized AB cells of the same genotype (Figures 5B
597 and 7A). However, only *pch-2* mutants significantly affect cell cycle timing in unperturbed
598 P_1 cells, (Figure 5C); P_1 cells in *cmt-1* and *mad-1* mutants show accelerated cell cycle
599 timing but this is not significantly faster than control (Figures 5C and 7B). Further, we
600 don't detect significant acceleration of the cell cycle in P_1 cells of *pch-2;zyg-1*^{RNAi} or *mad-*
601 *1;zyg-1*^{RNAi} mutant embryos (Figure S4 and 7B). Given the rapidity of cell cycles in these
602 early embryos, it's possible that *ani-2*^{RNAi}*;zyg-1*^{RNAi} experiments provide greater
603 sensitivity to observe subtle accelerations in cell cycle timing and that some subset of
604 spindle checkpoint components, including PCH-2, CMT-1, MAD-1 and MAD-2 regulate
605 normal cell cycle timing in germline precursor cells, similar to the role of MAD-1 and
606 MAD-2 in germline mitotic nuclei (Gerhold *et al.*, 2015). Unfortunately, we cannot test
607 this with MAD-1 or MAD-2 since *mad-1* and *mad-2* mutants abolish the spindle
608 checkpoint response in *ani-2*^{RNAi}*;zyg-1*^{RNAi} embryos (Gerhold *et al.*, 2015) and Figure
609 1C). An alternative hypothesis that we do not favor is that only PCH-2 regulates cell

610 cycle timing in P_1 cells, in a mechanism independent of other spindle checkpoint
611 proteins.
612
613 Evolutionary analysis across phyla have revealed a close co-evolutionary relationship
614 between PCH-2 and its orthologs and HORMA domain containing proteins, including
615 CMT-1 and Mad2 (Vleugel *et al.*, 2012; van Hooff *et al.*, 2017). However, some
616 organisms that rely on the templated conversion of O-Mad2 to C-Mad2 to assemble the
617 MCC, such as budding and fission yeasts (Nezi *et al.*, 2006; Chao *et al.*, 2012) either
618 don't express their PCH-2 ortholog during mitosis (budding yeast) (San-Segundo and
619 Roeder, 1999) or don't have a PCH-2 ortholog in their genome (fission yeast) (Wu and
620 Burgess, 2006). This is potentially explained by cell volume: Both budding and fission
621 yeasts are two orders of magnitude smaller than mammalian cells and *C. elegans*
622 embryos. They also undergo closed mitosis, in which the nuclear envelope does not
623 break down, providing an additional opportunity to concentrate factors required for
624 mitosis. We propose that recruiting O-Mad2 to unattached kinetochores may not present
625 as great a challenge in these significantly smaller cells, making a factor required to
626 increase the local concentration of O-Mad2 at unattached kinetochores unnecessary.
627
628 An obvious question our experiments raise is how PCH-2 is enriched in P_1 cells.
629 Germline precursor cells are transcriptionally silent until gastrulation (Seydoux *et al.*,
630 1996) and sequencing of mRNA in early embryos shows that both CMT-1 and PCH-2
631 mRNA are not enriched in germline precursor cells (Tintori *et al.*, 2016), indicating that
632 enrichment of PCH-2 is likely to occur at the level of protein regulation. Understanding
633 this regulation, its control by developmental events and its effect on the relative levels of
634 O-Mad2 and C-Mad2 in different cell types promises to be an exciting area of
635 investigation.

636

637 **MATERIALS AND METHODS**

638

639 **Worms strains**

640 The *C. elegans* Bristol N2 (Brenner, 1974) was used as the wild-type strain. Most strains
641 were maintained at 20°C, except for *zyg-1(or297)* strains, which were maintained at
642 15°C. See Table S1 for the list of all the strains used in this study.

643

644 **Immunostaining**

645 Immunostaining was performed on adult worms 48h after L4, as described in (Bhalla and
646 Dernburg, 2005). The antibodies used were rabbit anti-MAD-2 (1/500; (Essex *et al.*,
647 2009) and mouse anti-MAb414 (1/400; (Davis and Blobel, 1986). Secondary antibodies
648 were Alexa Fluor 488 anti-rabbit (Invitrogen) and Cy3 anti-mouse (Jackson
649 ImmunoResearch Laboratories, Inc.) diluted at 1:500. Antibody against MAD-2 was a gift
650 from A. Desai (Ludwig Institute/University of California, San Diego, La Jolla, CA).

651

652 Images were acquired on a DeltaVision Personal DV microscope (GE Healthcare)
653 equipped with a 100× NA 1.40 oil-immersion objective (Olympus), a short ARC xenon
654 lamp (GE Healthcare) and using a CoolSNAP charge-coupled camera (Roper Scientific).
655 Z-stacks were collected at 0.2 µm Z-spacing and processed by constrained, iterative
656 deconvolution. Imaging, image scaling, and analysis were performed using functions in
657 the softWoRx software package (GE Healthcare). Projections were calculated by a
658 maximum intensity algorithm. Composite images were assembled and some false
659 coloring was performed with Fiji.

660

661 **Live imaging of 2-cell embryos**

662 For live imaging of 2-cell embryos, worms were dissected on glass coverslips in egg
663 buffer and then mounted on 2% agar pads. Images were acquired every 1 minute or 20
664 seconds on a DeltaVision Personal DV microscope as described in the previous section;
665 except that the distance between two planes was 2 μm. Mitotic timing was measured
666 from NEBD to OCC as described in (Nelson *et al.*, 2015). Cell volumes were measured
667 as described in (Galli and Morgan, 2016). To measure the nuclear area, a sum
668 projection of the embryo was generated 1 minute before chromosomes began to
669 condense and the area was measured with Fiji (Figure S3A).
670
671 **Live imaging of embryogenesis**
672 After treatment with *perm-1*^{RNAi} (see below), worms were dissected onto a coverslip with
673 egg salt buffer (118 mM NaCl, 48 mM KCl) supplemented with 10 mM PIPES pH 7.3, 1
674 mM ATP and 10 mM sucrose. Embryos and adult carcasses were transferred into a well
675 of an 8-well plate (ibidi 1 μ-Slide 8 Well Glass bottom) that had been freshly coated with
676 0.1% Poly-L-Lysine solution (Sigma P8920) and extensively washed. Time-lapse videos
677 were acquired with a Solamere spinning disk confocal system piloted by μManager
678 software (Edelstein *et al.*, 2014) and equipped with a Yokogawa CSUX-1 scan head, a
679 Nikon (Garden City, NY) TE2000-E inverted stand, a Hamamatsu ImageEM ×2 camera,
680 LX/MAS 489 nm and LS/MAS 561 nm laser, and Plan Apo ×60/1.4 numerical aperture
681 oil objective. Acquisition times per frame were 50 ms using 5% of the lasers power for
682 both channels, and images were obtained as stacks of planes at 2 μm intervals taken
683 every 1 minute. Nocodazole was added from a 5X stock to a final concentration of 50 μM
684 after the first time point. Mitotic timing was measured from NEBD to DECON as
685 described in (Essex *et al.*, 2009).
686

687 To image embryogenesis in *zyg-1(or297)* mutants, images were generated under the
688 same conditions as previously described for the live imaging of 2-cell embryos with a few
689 modifications: Images were acquired every 20 seconds on a DeltaVision Personal DV
690 microscope in a room heated to 26°C. Mitotic timing was measured from NEBD to
691 DECON as described in (Essex *et al.*, 2009).
692
693 **Quantification of fluorescence intensity**
694 To quantify GFP::MAD-2 and PCH-2::GFP levels, images were generated under the
695 same conditions as previously described for the live imaging of 2-cell embryos with a few
696 modifications: only the area defined by the GFP cloud and mitotic chromosomes was
697 imaged, the interval between the four planes was 1 µm and images were collected every
698 20 seconds. Quantification of fluorescence at kinetochores was performed in Fiji as
699 described in (Moyle *et al.*, 2014; Nelson *et al.*, 2015). Briefly, maximum intensity
700 projections of both mCh::H2B and GFP fusion proteins were made after the pseudo-
701 metaphase plate was generated. The image was rotated so the metaphase plate was
702 vertical, channels were split, and the maximum GFP pixel was identified using the
703 process function within a box on the unattached side of the metaphase plate. In the
704 same x-plane, the maximum mCh::H2B pixel was found. The width was changed to 12
705 pixels and the maximum GFP signal intensity was recorded in this 12 pixel window
706 centered at the mCherry maxima. The background GFP signal was calculated by taking
707 the average GFP intensity of a 4 pixel box in the same x-plane, 8 pixels away from the
708 maximum mCherry on the opposite side of the pseudo-metaphase plate to the maximum
709 GFP (i.e. the attached side). This background GFP was then subtracted from the
710 maximum to measure the kinetochore bound GFP fusion intensity. Fluorescence around
711 mitotic chromosomes was quantified as described in (Galli and Morgan, 2016). Sum
712 intensity projections were generated and fluorescence in the area around mitotic

713 chromosomes was measured in Fiji. Background fluorescence was measured in a 30
714 pixel band around this “cloud” and subtracted from the initial fluorescence intensity to
715 determine the final fluorescence value. In some of our movies, identifying a clear
716 metaphase plate was more difficult in AB than P_1 cells. Therefore, to ensure that we
717 were quantifying PCH-2::GFP fluorescence around mitotic chromosomes at the same
718 stage in mitosis in these two cell types, PCH-2::GFP was quantified in frames that were
719 normalized relative to NEBD and mitotic exit. To measure the cell volume, one Z-stack of
720 the entire cell was taken at NEBD at 2 µm Z-spacing.
721
722 **Feeding RNA interference (RNAi)**
723 *C. elegans* strains were fed HT115 bacteria expressing the desired dsRNA after IPTG
724 induction. Bacterial strains containing RNAi vectors were cultured overnight at 37°C,
725 centrifuged, and the pellet was resuspended in 1/50 of the original volume. 100 µl of
726 concentrated culture was spotted onto a nematode growth medium (NGM) plate
727 containing 1 mM IPTG and 50 µg/µl of kanamycin or carbenicillin and the plate was
728 incubated overnight at 37°C.
729
730 For *ani-2* RNAi, gravid adults were bleached onto the RNAi plate and their progeny was
731 allowed to develop at 20°C during 2.5 days. Then, L4s were transferred to a fresh plate
732 containing OP50 or *zyg-1* RNAi bacteria.
733
734 For *zyg-1* RNAi, L4s were transferred (from an OP50 or *ani-2* RNAi plate) onto a *zyg-1*
735 RNAi plate and cultured 1.5 days at 20°C.
736
737 For *perm-1* RNAi, young adults (8h post L4) were incubated onto *perm-1* RNAi plates for
738 16-20 hours at 15°C.

739

740 For *par-1, par-6* and *gpr-1/2* RNAi, gravid adults were bleached onto control RNAi
741 (L4440) plates and their progeny were allowed to develop at 15°C for 3 days. L4s were
742 then transferred onto *par-1, par-6, gpr-1/2* RNAi or control RNAi plates and incubated at
743 15°C for 3 days. For *gpr-1/2* RNAi, "small" AB cells were identified by whether their area
744 was at least one standard deviation lower than the average of control AB cells and
745 "large" P_1 cells were identified by whether their area was at least one standard deviation
746 higher than the average of control P_1 cells.

747

748 **Statistical Analysis**

749 All statistical analysis was performed using GrapPad Prism version 6 for Macintosh,
750 including linear regression analysis and assessing significance of this data (Figures 1C,
751 2B, 3C, 5A, 5B, 7A, S1C, and S1D). For comparing two means, significance was
752 assessed by performing two-tailed t-tests (Figures 6C, S5B, S5D, S6B, S6C, S6D, and
753 S7A). In graphs in which multiple means were tested, we performed ANOVA analysis
754 with the Sidak post-hoc test (Figures 1D, 5C, 6A, 6E, 7B, 7D, S4A, S8A, S8B, and s8D).
755 In all graphs, a * indicates a p value < 0.05, ** indicates a p value < 0.01 and *** a p
756 value < 0.0001.

757

758 **ACKNOWLEDGEMENTS**

759

760 We would like to thank Arshad Desai, Karen Oegema, Susan Strome and David Morgan
761 for valuable strains and reagents. This work was supported by the NIH (grant numbers
762 T32GM008646 [C.R.N. and A.R.] and R01GM097144 [N.B.]). Some strains were
763 provided by the CGC, which is funded by NIH Office of Research Infrastructure
764 Programs (P40 OD010440).

CONTRIBUTIONS

Conceptualization and Methodology, L.D., A.E.R., C.R.N. and N.B.; Investigation, L.D., A.E.R., and C.R.N.; Writing - Original Draft, L.D. and N.B.; Writing - Review & Editing, L.D., A.E.R., C.R.N. and N.B.; Supervision and Funding Acquisition, N.B.

COMPETING INTERESTS

The authors declare no competing interests.

775 **REFERENCES**

776 Alfieri, C., Chang, L., and Barford, D. (2018). Mechanism for remodelling of the cell cycle
777 checkpoint protein MAD2 by the ATPase TRIP13. Nature *559*, 274-278.

778 Aravind, L., and Koonin, E.V. (1998). The HORMA domain: a common structural
779 denominator in mitotic checkpoints, chromosome synapsis and DNA repair. Trends
780 Biochem Sci *23*, 284-286.

781 Bhalla, N., and Dernburg, A.F. (2005). A conserved checkpoint monitors meiotic
782 chromosome synapsis in Caenorhabditis elegans. Science *310*, 1683-1686.

783 Bohr, T., Nelson, C.R., Klee, E., and Bhalla, N. (2015). Spindle assembly checkpoint
784 proteins regulate and monitor meiotic synapsis in C. elegans. J Cell Biol *211*, 233-242.

785 Brenner, S. (1974). The genetics of Caenorhabditis elegans. Genetics *77*, 71-94.

786 Brulotte, M.L., Jeong, B.C., Li, F., Li, B., Yu, E.B., Wu, Q., Brautigam, C.A., Yu, H., and
787 Luo, X. (2017). Mechanistic insight into TRIP13-catalyzed Mad2 structural transition and
788 spindle checkpoint silencing. Nat Commun *8*, 1956.

789 Carvalho, A., Olson, S.K., Gutierrez, E., Zhang, K., Noble, L.B., Zanin, E., Desai, A.,
790 Groisman, A., and Oegema, K. (2011). Acute drug treatment in the early C. elegans
791 embryo. PLoS One *6*, e24656.

792 Chao, W.C., Kulkarni, K., Zhang, Z., Kong, E.H., and Barford, D. (2012). Structure of the
793 mitotic checkpoint complex. Nature *484*, 208-213.

794 Chen, R.H., Shevchenko, A., Mann, M., and Murray, A.W. (1998). Spindle checkpoint
795 protein Xmad1 recruits Xmad2 to unattached kinetochores. J Cell Biol *143*, 283-295.

796 Chen, R.H., Waters, J.C., Salmon, E.D., and Murray, A.W. (1996). Association of spindle
797 assembly checkpoint component XMAD2 with unattached kinetochores. Science *274*,
798 242-246.

799 Chenevert, J., Roca, M., Besnardeau, L., Ruggiero, A., Nabi, D., McDougall, A., Copley,
800 R.R., Christians, E., and Castagnetti, S. (2019). The spindle assembly checkpoint
801 functions during early development in non-chordate embryos. bioRxiv.
802 Collin, P., Nashchekina, O., Walker, R., and Pines, J. (2013). The spindle assembly
803 checkpoint works like a rheostat rather than a toggle switch. Nat Cell Biol *15*, 1378-1385.
804 Colombo, K., Grill, S.W., Kimple, R.J., Willard, F.S., Siderovski, D.P., and Gonczy, P.
805 (2003). Translation of polarity cues into asymmetric spindle positioning in Caenorhabditis
806 elegans embryos. Science *300*, 1957-1961.
807 Davis, L.I., and Blobel, G. (1986). Identification and characterization of a nuclear pore
808 complex protein. Cell *45*, 699-709.
809 De Antoni, A., Pearson, C.G., Cimini, D., Canman, J.C., Sala, V., Nezi, L., Mapelli, M.,
810 Sironi, L., Faretta, M., Salmon, E.D., and Musacchio, A. (2005). The Mad1/Mad2
811 complex as a template for Mad2 activation in the spindle assembly checkpoint. Current
812 biology : CB *15*, 214-225.
813 Dick, A.E., and Gerlich, D.W. (2013). Kinetic framework of spindle assembly checkpoint
814 signalling. Nat Cell Biol *15*, 1370-1377.
815 Edelstein, A.D., Tsuchida, M.A., Amodaj, N., Pinkard, H., Vale, R.D., and Stuurman, N.
816 (2014). Advanced methods of microscope control using muManager software. J Biol
817 Methods *1*.
818 Essex, A., Dammermann, A., Lewellyn, L., Oegema, K., and Desai, A. (2009).
819 Systematic analysis in Caenorhabditis elegans reveals that the spindle checkpoint is
820 composed of two largely independent branches. Mol Biol Cell *20*, 1252-1267.
821 Eytan, E., Wang, K., Miniowitz-Shemtov, S., Sitry-Shevah, D., Kaisari, S., Yen, T.J., Liu,
822 S.T., and Hershko, A. (2014). Disassembly of mitotic checkpoint complexes by the joint
823 action of the AAA-ATPase TRIP13 and p31(comet). Proc Natl Acad Sci U S A *111*,
824 12019-12024.

825 Fava, L.L., Kaulich, M., Nigg, E.A., and Santamaria, A. (2011). Probing the in vivo
826 function of Mad1:C-Mad2 in the spindle assembly checkpoint. EMBO J *30*, 3322-3336.
827 Galli, M., and Morgan, D.O. (2016). Cell Size Determines the Strength of the Spindle
828 Assembly Checkpoint during Embryonic Development. Dev Cell *36*, 344-352.
829 Gerhold, A.R., Poupart, V., Labbe, J.C., and Maddox, P.S. (2018). Spindle assembly
830 checkpoint strength is linked to cell fate in the Caenorhabditis elegans embryo. Mol Biol
831 Cell *29*, 1435-1448.
832 Gerhold, A.R., Ryan, J., Vallee-Trudeau, J.N., Dorn, J.F., Labbe, J.C., and Maddox, P.S.
833 (2015). Investigating the regulation of stem and progenitor cell mitotic progression by in
834 situ imaging. Curr Biol *25*, 1123-1134.
835 Goldstein, B., and Macara, I.G. (2007). The PAR proteins: fundamental players in animal
836 cell polarization. Dev Cell *13*, 609-622.
837 Gotta, M., Dong, Y., Peterson, Y.K., Lanier, S.M., and Ahringer, J. (2003).
838 Asymmetrically distributed C. elegans homologs of AGS3/PINS control spindle position
839 in the early embryo. Curr Biol *13*, 1029-1037.
840 Guo, S., and Kemphues, K.J. (1995). par-1, a gene required for establishing polarity in
841 C. elegans embryos, encodes a putative Ser/Thr kinase that is asymmetrically
842 distributed. Cell *81*, 611-620.
843 Hung, T.J., and Kemphues, K.J. (1999). PAR-6 is a conserved PDZ domain-containing
844 protein that colocalizes with PAR-3 in Caenorhabditis elegans embryos. Development
845 *126*, 127-135.
846 Kitagawa, R., and Rose, A.M. (1999). Components of the spindle-assembly checkpoint
847 are essential in Caenorhabditis elegans. Nat Cell Biol *1*, 514-521.
848 Kyogoku, H., and Kitajima, T.S. (2017). Large Cytoplasm Is Linked to the Error-Prone
849 Nature of Oocytes. Dev Cell *41*, 287-298 e284.

850 Lara-Gonzalez, P., Moyle, M.W., Budrewicz, J., Mendoza-Lopez, J., Oegema, K., and
851 Desai, A. (2019). The G2-to-M Transition Is Ensured by a Dual Mechanism that Protects
852 Cyclin B from Degradation by Cdc20-Activated APC/C. Dev Cell *51*, 313-325 e310.
853 Lawrence, K.S., Chau, T., and Engebrecht, J. (2015). DNA damage response and
854 spindle assembly checkpoint function throughout the cell cycle to ensure genomic
855 integrity. PLoS Genet *11*, e1005150.
856 Li, Y., and Benezra, R. (1996). Identification of a human mitotic checkpoint gene:
857 hsMAD2. Science *274*, 246-248.
858 Luo, X., Tang, Z., Rizo, J., and Yu, H. (2002). The Mad2 spindle checkpoint protein
859 undergoes similar major conformational changes upon binding to either Mad1 or Cdc20.
860 Mol Cell *9*, 59-71.
861 Luo, X., Tang, Z., Xia, G., Wassmann, K., Matsumoto, T., Rizo, J., and Yu, H. (2004).
862 The Mad2 spindle checkpoint protein has two distinct natively folded states. Nat Struct
863 Mol Biol *11*, 338-345.
864 Ma, H.T., and Poon, R.Y. (2016). TRIP13 Regulates Both the Activation and Inactivation
865 of the Spindle-Assembly Checkpoint. Cell Rep *14*, 1086-1099.
866 Ma, H.T., and Poon, R.Y.C. (2018). TRIP13 Functions in the Establishment of the
867 Spindle Assembly Checkpoint by Replenishing O-MAD2. Cell Rep *22*, 1439-1450.
868 Maddox, A.S., Habermann, B., Desai, A., and Oegema, K. (2005). Distinct roles for two
869 C. elegans anillins in the gonad and early embryo. Development *132*, 2837-2848.
870 Mariani, L., Chiroli, E., Nezi, L., Muller, H., Piatti, S., Musacchio, A., and Ciliberto, A.
871 (2012). Role of the Mad2 dimerization interface in the spindle assembly checkpoint
872 independent of kinetochores. Curr Biol *22*, 1900-1908.
873 Marks, D.H., Thomas, R., Chin, Y., Shah, R., Khoo, C., and Benezra, R. (2017). Mad2
874 Overexpression Uncovers a Critical Role for TRIP13 in Mitotic Exit. Cell Rep *19*, 1832-
875 1845.

876 Meraldi, P., Draviam, V.M., and Sorger, P.K. (2004). Timing and checkpoints in the
877 regulation of mitotic progression. Dev Cell *7*, 45-60.
878 Miniowitz-Shemtov, S., Eytan, E., Kaisari, S., Sitry-Shevah, D., and Hershko, A. (2015).
879 Mode of interaction of TRIP13 AAA-ATPase with the Mad2-binding protein p31comet
880 and with mitotic checkpoint complexes. Proc Natl Acad Sci U S A *112*, 11536-11540.
881 Moyle, M.W., Kim, T., Hattersley, N., Espeut, J., Cheerambathur, D.K., Oegema, K., and
882 Desai, A. (2014). A Bub1-Mad1 interaction targets the Mad1-Mad2 complex to
883 unattached kinetochores to initiate the spindle checkpoint. J Cell Biol *204*, 647-657.
884 Nelson, C.R., Hwang, T., Chen, P.H., and Bhalla, N. (2015). TRIP13PCH-2 promotes
885 Mad2 localization to unattached kinetochores in the spindle checkpoint response. J Cell
886 Biol *211*, 503-516.
887 Nezi, L., Rancati, G., De Antoni, A., Pasqualato, S., Piatti, S., and Musacchio, A. (2006).
888 Accumulation of Mad2-Cdc20 complex during spindle checkpoint activation requires
889 binding of open and closed conformers of Mad2 in Saccharomyces cerevisiae. J Cell
890 Biol *174*, 39-51.
891 Nystul, T.G., Goldmark, J.P., Padilla, P.A., and Roth, M.B. (2003). Suspended animation
892 in C. elegans requires the spindle checkpoint. Science *302*, 1038-1041.
893 O'Connell, K.F., Caron, C., Kopish, K.R., Hurd, D.D., Kemphues, K.J., Li, Y., and White,
894 J.G. (2001). The C. elegans zyg-1 gene encodes a regulator of centrosome duplication
895 with distinct maternal and paternal roles in the embryo. Cell *105*, 547-558.
896 O'Rourke, S.M., Carter, C., Carter, L., Christensen, S.N., Jones, M.P., Nash, B., Price,
897 M.H., Turnbull, D.W., Garner, A.R., Hamill, D.R., Osterberg, V.R., Lyczak, R., Madison,
898 E.E., Nguyen, M.H., Sandberg, N.A., Sedghi, N., Willis, J.H., Yochem, J., Johnson, E.A.,
899 and Bowerman, B. (2011). A survey of new temperature-sensitive, embryonic-lethal
900 mutations in C. elegans: 24 alleles of thirteen genes. PLoS One *6*, e16644.

901 Rodriguez-Bravo, V., Maciejowski, J., Corona, J., Buch, H.K., Collin, P., Kanemaki, M.T.,
902 Shah, J.V., and Jallepalli, P.V. (2014). Nuclear pores protect genome integrity by
903 assembling a premitotic and Mad1-dependent anaphase inhibitor. Cell *156*, 1017-1031.
904 Rose, L., and Gonczy, P. (2014). Polarity establishment, asymmetric division and
905 segregation of fate determinants in early C. elegans embryos. WormBook, 1-43.
906 Rosenberg, S.C., and Corbett, K.D. (2015). The multifaceted roles of the HORMA
907 domain in cellular signaling. J Cell Biol *211*, 745-755.
908 San-Segundo, P.A., and Roeder, G.S. (1999). Pch2 links chromatin silencing to meiotic
909 checkpoint control. Cell *97*, 313-324.
910 Seydoux, G., Mello, C.C., Pettitt, J., Wood, W.B., Priess, J.R., and Fire, A. (1996).
911 Repression of gene expression in the embryonic germ lineage of C. elegans. Nature
912 *382*, 713-716.
913 Simonetta, M., Manzoni, R., Mosca, R., Mapelli, M., Massimiliano, L., Vink, M., Novak,
914 B., Musacchio, A., and Ciliberto, A. (2009). The influence of catalysis on mad2 activation
915 dynamics. PLoS Biol *7*, e10.
916 Sironi, L., Mapelli, M., Knapp, S., De Antoni, A., Jeang, K.T., and Musacchio, A. (2002).
917 Crystal structure of the tetrameric Mad1-Mad2 core complex: implications of a 'safety
918 belt' binding mechanism for the spindle checkpoint. EMBO J *21*, 2496-2506.
919 Sironi, L., Melixetian, M., Faretta, M., Prosperini, E., Helin, K., and Musacchio, A. (2001).
920 Mad2 binding to Mad1 and Cdc20, rather than oligomerization, is required for the spindle
921 checkpoint. EMBO J *20*, 6371-6382.
922 Srinivasan, D.G., Fisk, R.M., Xu, H., and van den Heuvel, S. (2003). A complex of LIN-5
923 and GPR proteins regulates G protein signaling and spindle function in C elegans.
924 Genes Dev *17*, 1225-1239.

925 Stein, K.K., Davis, E.S., Hays, T., and Golden, A. (2007). Components of the spindle
926 assembly checkpoint regulate the anaphase-promoting complex during meiosis in
927 Caenorhabditis elegans. Genetics *175*, 107-123.
928 Sudakin, V., Chan, G.K., and Yen, T.J. (2001). Checkpoint inhibition of the APC/C in
929 HeLa cells is mediated by a complex of BUBR1, BUB3, CDC20, and MAD2. J Cell Biol
930 *154*, 925-936.
931 Tintori, S.C., Osborne Nishimura, E., Golden, P., Lieb, J.D., and Goldstein, B. (2016). A
932 Transcriptional Lineage of the Early C. elegans Embryo. Dev Cell *38*, 430-444.
933 Tipton, A.R., Wang, K., Oladimeji, P., Sufi, S., Gu, Z., and Liu, S.T. (2012). Identification
934 of novel mitosis regulators through data mining with human centromere/kinetochore
935 proteins as group queries. BMC Cell Biol *13*, 15.
936 Vader, G. (2015). Pch2(TRIP13): controlling cell division through regulation of HORMA
937 domains. Chromosoma *124*, 333-339.
938 van Hooff, J.J., Tromer, E., van Wijk, L.M., Snel, B., and Kops, G.J. (2017). Evolutionary
939 dynamics of the kinetochore network in eukaryotes as revealed by comparative
940 genomics. EMBO Rep.
941 Vazquez-Diez, C., Paim, L.M.G., and FitzHarris, G. (2019). Cell-Size-Independent
942 Spindle Checkpoint Failure Underlies Chromosome Segregation Error in Mouse
943 Embryos. Curr Biol *29*, 865-873 e863.
944 Vleugel, M., Hoogendoorn, E., Snel, B., and Kops, G.J. (2012). Evolution and function of
945 the mitotic checkpoint. Dev Cell *23*, 239-250.
946 Wang, K., Sturt-Gillespie, B., Hittle, J.C., Macdonald, D., Chan, G.K., Yen, T.J., and Liu,
947 S.T. (2014). Thyroid hormone receptor interacting protein 13 (TRIP13) AAA-ATPase is a
948 novel mitotic checkpoint-silencing protein. J Biol Chem *289*, 23928-23937.
949 Wu, H.Y., and Burgess, S.M. (2006). Two distinct surveillance mechanisms monitor
950 meiotic chromosome metabolism in budding yeast. Curr Biol *16*, 2473-2479.

951 Ye, Q., Rosenberg, S.C., Moeller, A., Speir, J.A., Su, T.Y., and Corbett, K.D. (2015).
952 TRIP13 is a protein-remodeling AAA+ ATPase that catalyzes MAD2 conformation
953 switching. eLife *4*.
954 Yost, S., de Wolf, B., Hanks, S., Zachariou, A., Marcozzi, C., Clarke, M., de Voer, R.M.,
955 Etemad, B., Uijttewaal, E., Ramsay, E., Wylie, H., Elliott, A., Picton, S., Smith, A.,
956 Smithson, S., Seal, S., Ruark, E., Houge, G., Pines, J., Kops, G., and Rahman, N.
957 (2017). Biallelic TRIP13 mutations predispose to Wilms tumor and chromosome
958 missegregation. Nat Genet.
959

960 **Figure Legends**

961

962 **Figure 1: PCH-2 becomes dispensable for the spindle checkpoint response in**

963 **somatic cells experimentally reduced in size**

964 (A) Images of wildtype-sized and small *ani-2*^{RNAi} 2-cell embryos. Scale bar indicates 5

965 µm. (B) Cartoon of wildtype-sized and small *ani-2*^{RNAi} 2-cell embryos treated with *zyg-*

966 *1*^{RNAi}. (C) Mitotic timing, as measured from nuclear envelope breakdown (NEBD) to the

967 onset of cortical contractility (OCC), in AB cells of control, *pch-2* and *mad-1* mutant

968 embryos plotted against cell volume. Lines represent least-squares regression models

969 with 95% confidence intervals (gray shaded areas) for each set of data. Equations and p

970 values indicating whether slopes are significantly non-zero for each model are: *ani-*

971 *2*^{RNAi}*;zyg-1*^{RNAi} (blue): y=-1.117x+11.15 and p < 0.0001; *pch-2;ani-2*^{RNAi}*;zyg-1*^{RNAi} (red):

972 y=-1.264x+10.50 and p < 0.0001; *mad-1;ani-2*^{RNAi}*;zyg-1*^{RNAi} (green): y=-0.1709x+4.468

973 and p = 0.4197. (D) Data from (C) partitioned into three categories: wild-type sized

974 embryos (more than 5 x 10^3 µm^3), medium sized embryos (between 3.3 x 10^3 µm^3 and 5

975 x 10^3 µm^3) and small embryos (less than 3.3 x 10^3 µm^3). Error bars are 95% confidence

976 intervals. In all graphs, a * indicates a p value < 0.05, ** indicates a p value < 0.01 and

977 *** a p value < 0.0001.

978

979 **Figure 2: MAD-2 recruitment is partially restored to unattached kinetochores in**

980 ***pch-2* mutant somatic cells experimentally reduced in size**

981 (A) Cartoon and images of GFP::MAD-2 recruitment to unattached kinetochores in AB

982 cells of control and *pch-2* AB cells treated with *ani-2* and *zyg-1* RNAi. Scale bar indicates

983 1 µm. (B) Quantification of kinetochore bound GFP::MAD-2 in control and *pch-2* AB cells

984 plotted against cell volume. Lines represent least-squares regression models with 95%

985 confidence intervals (gray shaded areas) for each set of data. Equations and p values

986 indicating whether slopes are significantly non-zero for each model are: *ani-2*^{RNAi}*;zyg-*
987 *1*^{RNAi} (blue): y=1.531x+5.024 and p = 0.0115; *pch-2;ani-2*^{RNAi}*;zyg-1*^{RNAi} (red): y=-
988 1.384x+7.911 and p = 0.0384.
989
990 **Figure 3: MAD-2 dosage controls checkpoint strength**
991 (A) Immunostaining of MAD-2 and nuclear pore complex components (NPCs) shows
992 MAD-2 localized in the nucleus and at the nuclear envelope during interphase. Scale bar
993 indicates 5 μm. (B) Model depicting how a decrease in cell volume might result in an
994 increase in the local concentration of O-Mad2 in *ani-2*^{RNAi}*;zyg-1*^{RNAi} embryos, in contrast
995 to *zyg-1*^{RNAi} embryos. (C) Mitotic timing, as measured from nuclear envelope breakdown
996 (NEBD) to the onset of cortical contractility (OCC), in AB cells of control and *mad-2/+*
997 mutant embryos plotted against cell volume. Lines represent least-squares regression
998 models with 95% confidence intervals (gray shaded areas) for each set of data.
999 Equations and p values indicating whether slopes are significantly non-zero for each
1000 model are: control (dark purple): y=-1.302x+8.477 and p = 0.0002; *mad-2/+* (light
1001 purple): y=-0.3171x+4.402 and p = 0.0395.
1002
1003 **Figure 4: PCH-2 regulates spindle checkpoint strength during embryogenesis**
1004 (A) Mitotic timing, as measured from nuclear envelope breakdown (NEBD) to
1005 decondensation of chromatin (DECON), in control, *pch-2* and *san-1* mutant embryos
1006 treated with *perm-1* RNAi and DMSO or nocodazole at different developmental stages
1007 (4- and 16-cell embryos). (B) Mitotic timing in control and *pch-2* mutant embryos
1008 overexpressing GFP::MAD-2 and treated with *perm-1* RNAi and either DMSO or
1009 nocodazole at different developmental stages (4- and 16-cell embryos). (C) Mitotic
1010 timing in *zyg-1*^{ts} and *pch-2;zyg-1*^{ts} mutant embryos at different developmental stages (2-,
1011 4- and 8-cell embryos). All error bars are 95% confidence intervals.

1012

1013 **Figure 5: PCH-2 is responsible for the stronger spindle checkpoint in the germline**

1014 **lineage**

1015 Mitotic timing, as measured from nuclear envelope breakdown (NEBD) to the onset of

1016 cortical contractility (OCC), in AB and P_1 cells plotted against cell volume in control *ani-*

1017 *2^{RNAi};zyg-1^{RNAi}* embryos (A) or *pch-2;ani-2^{RNAi};zyg-1^{RNAi}* (B) embryos. Lines represent

1018 least-squares regression models with 95% confidence intervals (gray shaded areas) for

1019 each set of data. Equations and p values indicating whether slopes are significantly non-

1020 zero for each model are: *ani-2^{RNAi};zyg-1^{RNAi}* AB (dark blue): y=-1.117x+11.15 and p <

1021 0.0001; *ani-2^{RNAi};zyg-1^{RNAi}* P_1 (light blue): y=-8.047x+32.27 and p = 0.0021; *pch-2;ani-*

1022 *2^{RNAi};zyg-1^{RNAi}* AB (red): y=-1.264x+10.50 and p < 0.0001; *pch-2;ani-2^{RNAi};zyg-1^{RNAi}* P_1

1023 (pink): y=-1.218x+7.75 and p = 0.0125. Data for AB cells in both control and *pch-2*

1024 mutants is the same as in Figure 1C. (C) Mitotic timing of AB and P_1 cells in control, *pch-*

1025 *2* and *mad-1* mutants during unperturbed divisions. Error bars are 95% confidence

1026 intervals.

1027

1028 **Figure 6: PCH-2's enrichment around mitotic chromosomes in P_1 cells depends on**

1029 **PAR-1**

1030 (A) Mitotic timing of control embryos and embryos expressing PCH-2::GFP during

1031 unperturbed divisions or in the presence of monopolar spindles. (B) Cartoon and images

1032 of PCH-2::GFP localization around mitotic chromosomes in AB and P_1 cells of 2-cell

1033 embryos. Scale bar indicates 5 µm. (C) Quantification of PCH-2::GFP fluorescence in

1034 AB and P_1 cells. (D) Cartoon and images of PCH-2::GFP localization around mitotic

1035 chromosomes in AB and P_1 cells of control RNAi and *par-1^{RNAi}* 2-cell embryos. (E)

1036 Quantification of PCH-2::GFP fluorescence in AB and P_1 cells of *par-1^{RNAi}* embryos. All

1037 error bars are 95% confidence intervals. NS indicates not significant.

1038

1039 **Figure 7: The stronger checkpoint in P_1 cells depends on CMT-1**

1040 (A) Mitotic timing, as measured from nuclear envelope breakdown (NEBD) to the onset
1041 of cortical contractility (OCC), in AB and P_1 cells plotted against cell volume in *cmt-1;ani-*
1042 *2^{RNAi};zyg-1^{RNAi}* embryos. Lines represent least-squares regression models with 95%
1043 confidence intervals (gray shaded areas) for each set of data. The opaque blue line
1044 represents the regression model of the control AB data from Figure 1C. Equations and p
1045 values indicating whether slopes are significantly non-zero for each model are: *cmt-*
1046 *1;ani-2^{RNAi};zyg-1^{RNAi}* AB (dark green): y=-0.713x+7.44 and p = 0.0050; *cmt-1;ani-*
1047 *2^{RNAi};zyg-1^{RNAi}* P_1 (light green): y=-0.6767x+5.291 and p = 0.0452. (B) Mitotic timing of
1048 control, *cmt-1* and *mad-1* mutant embryos during unperturbed divisions or in the
1049 presence of monopolar spindles. (C) Cartoon and images of PCH-2::GFP localization
1050 around mitotic chromosomes in AB and P_1 cells of *cmt-1* mutant embryos. Scale bar
1051 indicates 5 μm. (D) Quantification of PCH-2::GFP fluorescence in AB cells of control and
1052 *cmt-1* mutant embryos. (E) Quantification of PCH-2::GFP fluorescence in AB and P_1
1053 cells of *cmt-1* mutant embryos. All error bars are 95% confidence intervals. NS indicates
1054 not significant.

1055

1056 **Figure 8: Model**

1057 (A) A robust spindle checkpoint response in large cells requires the presence of PCH-2
1058 at unattached kinetochores to increase the local concentration O-MAD-2 at and near
1059 unattached kinetochores. (B) Reducing cell volume of 2-cell embryos increases the
1060 concentration of O-Mad-2 at and near unattached kinetochores, allowing a checkpoint
1061 response in the absence of PCH-2. (C) The enrichment of PCH-2 around mitotic
1062 chromosomes in P_1 cells results in a higher production of O-MAD-2, generating a
1063 stronger spindle checkpoint response in these cells.

1064

1065 **Figure S1: Related to Figure 1. The mitotic delay observed in *pch-2;ani-2^{RNAi};zyg-*
1066 ***1^{RNAi}* small cells is a spindle checkpoint response.**

1067 Cartoon of control and *ani-2^{RNAi}* 2-cell embryos (A) and an *ani-2^{RNAi};zyg-1^{RNAi}* 2-cell
1068 embryo (B). Mitotic timing in AB cells plotted against cell volume, during unperturbed
1069 mitosis (C) and in the presence of monopolar spindles. (D). Lines represent least-
1070 squares regression models for each set of data. For (C) equations and p values
1071 indicating whether slopes are significantly non-zero for each model are: *ani-2^{RNAi}* (blue):
1072 $y=-9.744\times10^{-3}x+3.001$ and $p = 0.6073$; *pch-2;ani-2^{RNAi}* (red): $y=-0.1315x+3.503$ and $p =$
1073 0.0483; *mad-1;ani-2^{RNAi}* (green): $y=-0.2944x+4.247$ and $p = 0.0251$. In (D), 95%
1074 confidence intervals are indicated by gray shaded areas and equations and p values
1075 indicating whether slopes are significantly non-zero for each model are: *san-1;ani-*
1076 *2^{RNAi};zyg-1^{RNAi}* P_1 (blue): $y=-0.4136x+5.535$ and $p = 0.1885$; *san-1;pch-2;ani-2^{RNAi};zyg-*
1077 *1^{RNAi}* P_1 (red): $y=-0.3541x+5.647$ and $p = 0.0643$. The regression model of *pch-2;ani-*
1078 *2^{RNAi};zyg-1^{RNAi}* embryos from Figure 1C is indicated by the opaque red line in (D) for
1079 comparison.

1080

1081 **Figure S2: Related to Figure 2: There is no difference in GFP::MAD-2 fluorescence**
1082 **around mitotic chromosomes in *ani-2^{RNAi};zyg-1^{RNAi}* embryos and *pch-2;ani-***
1083 ***2^{RNAi};zyg-1^{RNAi}* AB cells.**

1084 (A) Images of MAD-2::GFP in AB cells of control *ani-2^{RNAi};zyg-1^{RNAi}* embryos or *pch-*
1085 *2;ani-2^{RNAi};zyg-1^{RNAi}* embryos after NEBD. Scale bar indicates 5 µm. (B) Quantification of
1086 GFP::MAD-2 fluorescence around mitotic chromosomes in AB cells of control and *pch-2*
1087 embryos plotted against cell volume.

1088

1089 **Figure S3: Related to Figure 3. Nuclear volume does not scale with cell volume in**
1090 ***ani-2^{RNAi}* 2-cell embryos.**
1091 (A) Images of a large (top) and small (bottom) AB cell of *ani-2^{RNAi}* embryos. The nuclear
1092 area is indicated with a dashed yellow line. Scale bar indicates 5 μm. (B) Nuclear area
1093 plotted against cell volume.
1094
1095 **Figure S4: Related to Figure 5. PCH-2 is required for the spindle checkpoint in the**
1096 **germline lineage.**
1097 (A) Mitotic timing of control and *pch-2* mutant embryos during unperturbed divisions or in
1098 the presence of monopolar spindles. Data for control embryos is the same as Figure 7B.
1099 Error bars indicate 95% confidence intervals.
1100
1101 **Figure S5: Related to Figure 6. There is no difference in the amount of PCH-2::GFP**
1102 **or GFP::MAD-2 recruited to unattached kinetochores in AB and P_1 cells.**
1103 (A) Cartoon and images of PCH-2::GFP recruitment to unattached kinetochores in AB
1104 and P_1 cells of 2-cell embryos. Scale bar indicates 1 μm. (B) Quantification of PCH-
1105 2::GFP recruitment at unattached kinetochores in AB and P_1 cells. (C) Cartoon and
1106 images of GFP::MAD-2 recruitment to unattached kinetochores in AB and P_1 cells of 2-
1107 cell embryos. Scale bar indicates 1 μm. (D) Quantification of GFP::MAD-2 fluorescence
1108 at unattached kinetochores in AB and P_1 cells. All error bars are 95% confidence
1109 intervals. NS indicates not significant.
1110
1111 **Figure S6: Related to Figure 6. There is no difference in the amount of PCH-2::GFP**
1112 **around mitotic chromosomes in AB cells with bipolar or monopolar spindles.** (A)
1113 Cartoon and images of PCH-2::GFP localization around mitotic chromosomes in AB
1114 cells of 2-cell embryos. Scale bar indicates 5 μm. Yellow dashed circle indicates area of

1115 PCH-2::GFP fluorescence. (B) Quantification of PCH-2::GFP fluorescence in AB cells
1116 with bipolar spindles (control) or monopolar spindles (*zyg-1*^{RNAi}). (C) Quantification of
1117 area of PCH-2::GFP fluorescence in AB cells with bipolar spindles or monopolar
1118 spindles. (D) Quantification of integrated density of PCH-2::GFP fluorescence in AB cells
1119 with bipolar spindles or monopolar spindles. All error bars are 95% confidence intervals.
1120 NS indicates not significant.
1121
1122 **Figure S7: Related to Figure 6. PCH-2's enrichment in P1 cells is around**
1123 **chromosomes and does not depend on GPR-1/2.**
1124 (A) Quantification of PCH-2::GFP fluorescence in the cytoplasm of AB and P_1 cells. (B)
1125 Images of AB (left) and P_1 (right) cells after NEBD. Scale bar indicate 5 μm. (C)
1126 Quantification of cell area in AB and P_1 cells of control RNAi and *gpr-1/2*^{RNAi} 2-cell
1127 embryos. Red symbols indicate cells in which PCH-2::GFP fluorescence was quantified
1128 in (D). (D) Quantification of PCH-2::GFP fluorescence in AB and P_1 cells of control RNAi
1129 and *gpr-1/2*^{RNAi} embryos. (E) Cartoon and images of PCH-2::GFP localization around
1130 mitotic chromosomes in AB and P_1 cells of control RNAi and *gpr-1/2*^{RNAi} 2-cell embryos.
1131 Scale bars indicate 5 μm. Error bars are 95% confidence intervals. NS indicates not
1132 significant.
1133
1134 **Figure S8: Related to Figure 6. PCH-2's enrichment around mitotic chromosomes**
1135 **in P_1 cells depends on PAR-6.** (A and B) Quantification of cell area in AB and P_1 cells
1136 of control RNAi, *par-1*^{RNAi} and *par-6*^{RNAi} 2-cell embryos. (C) Cartoon and images of PCH-
1137 2::GFP localization around mitotic chromosomes in AB and P_1 cells of control RNAi and
1138 *par-6*^{RNAi} 2-cell embryos. Scale bars indicate 5 μm. (D) Quantification of PCH-2::GFP
1139 fluorescence in AB and P_1 cells of control RNAi and *par-6*^{RNAi} embryos. Error bars are
1140 95% confidence intervals. NS indicates not significant.

1141

1142 **Movie legends**

1143

1144 **Video 1**

1145 Mitosis in the AB cell of a wild-type sized control 2-cell embryo with monopolar spindles
1146 expressing GFH::PH and mCherry::H2B for visualization of the plasma membrane and
1147 the chromosomes, respectively (strain OD95). The timer starts at NEBD.

1148

1149 **Video 2**

1150 Mitosis in the AB cell of a small control 2-cell embryo with monopolar spindles
1151 expressing GFH::PH and mCherry::H2B for visualization of the plasma membrane and
1152 the chromosomes, respectively (strain OD95). The timer starts at NEBD.

1153

1154 **Video 3**

1155 Mitosis in the AB cell of a wild-type sized *pch-2(tm1458)* 2-cell embryo with monopolar
1156 spindles expressing GFH::PH and mCherry::H2B for visualization of the plasma
1157 membrane and the chromosomes, respectively (strain BHL575). The timer starts at
1158 NEBD.

1159

1160 **Video 4**

1161 Mitosis in the AB cell of a small *pch-2(tm1458*) 2-cell embryo with monopolar spindles
1162 expressing GFH::PH and mCherry::H2B for visualization of the plasma membrane and
1163 the chromosomes, respectively (strain BHL575). The timer starts at NEBD.

1164

1165 **Video 5**

1166 Mitosis in the P_1 cell of a wild-type sized control 2-cell embryo with monopolar spindles
1167 expressing GFH::PH and mCherry::H2B for visualization of the plasma membrane and
1168 the chromosomes, respectively (strain OD95). The timer starts at NEBD.
1169
1170 **Video 6**
1171 Mitosis in the P_1 cell of a small control 2-cell embryo with monopolar spindles expressing
1172 GFH::PH and mCherry::H2B for visualization of the plasma membrane and the
1173 chromosomes, respectively (strain OD95). The timer starts at NEBD.
1174
1175 **Video 7**
1176 Mitosis in the P_1 cell of a wild-type sized *pch-2(tm1458)* 2-cell embryo with monopolar
1177 spindles expressing GFH::PH and mCherry::H2B for visualization of the plasma
1178 membrane and the chromosomes, respectively (strain BHL575). The timer starts at
1179 NEBD.
1180
1181 **Video 8**
1182 Mitosis in the P_1 cell of a small *pch-2(tm1458)* 2-cell embryo with monopolar spindles
1183 expressing GFH::PH and mCherry::H2B for visualization of the plasma membrane and
1184 the chromosomes, respectively (strain BHL575). The timer starts at NEBD.
1185
1186 **Video 9**
1187 Mitosis in the AB cell of a wild-type sized *cmt-1(ok2879*) 2-cell embryo with monopolar
1188 spindles expressing GFH::PH and mCherry::H2B for visualization of the plasma
1189 membrane and the chromosomes, respectively (strain BHL608). The timer starts at
1190 NEBD.
1191

1192 **Video 10**

1193 Mitosis in the AB cell of a small *cmt-1(ok2879*) 2-cell embryo with monopolar spindles
1194 expressing GFH::PH and mCherry::H2B for visualization of the plasma membrane and
1195 the chromosomes, respectively (strain BHL608). The timer starts at NEBD.

1196

1197 **Video 11**

1198 Mitosis in the P_1 cell of a wild-type sized *cmt-1(ok2879*) 2-cell embryo with monopolar
1199 spindles expressing GFH::PH and mCherry::H2B for visualization of the plasma
1200 membrane and the chromosomes, respectively (strain BHL608). The timer starts at
1201 NEBD.

1202

1203 **Video 12**

1204 Mitosis in the P_1 cell of a small *cmt-1(ok2879*) 2-cell embryo with monopolar spindles
1205 expressing GFH::PH and mCherry::H2B for visualization of the plasma membrane and
1206 the chromosomes, respectively (strain BHL608). The timer starts at NEBD.

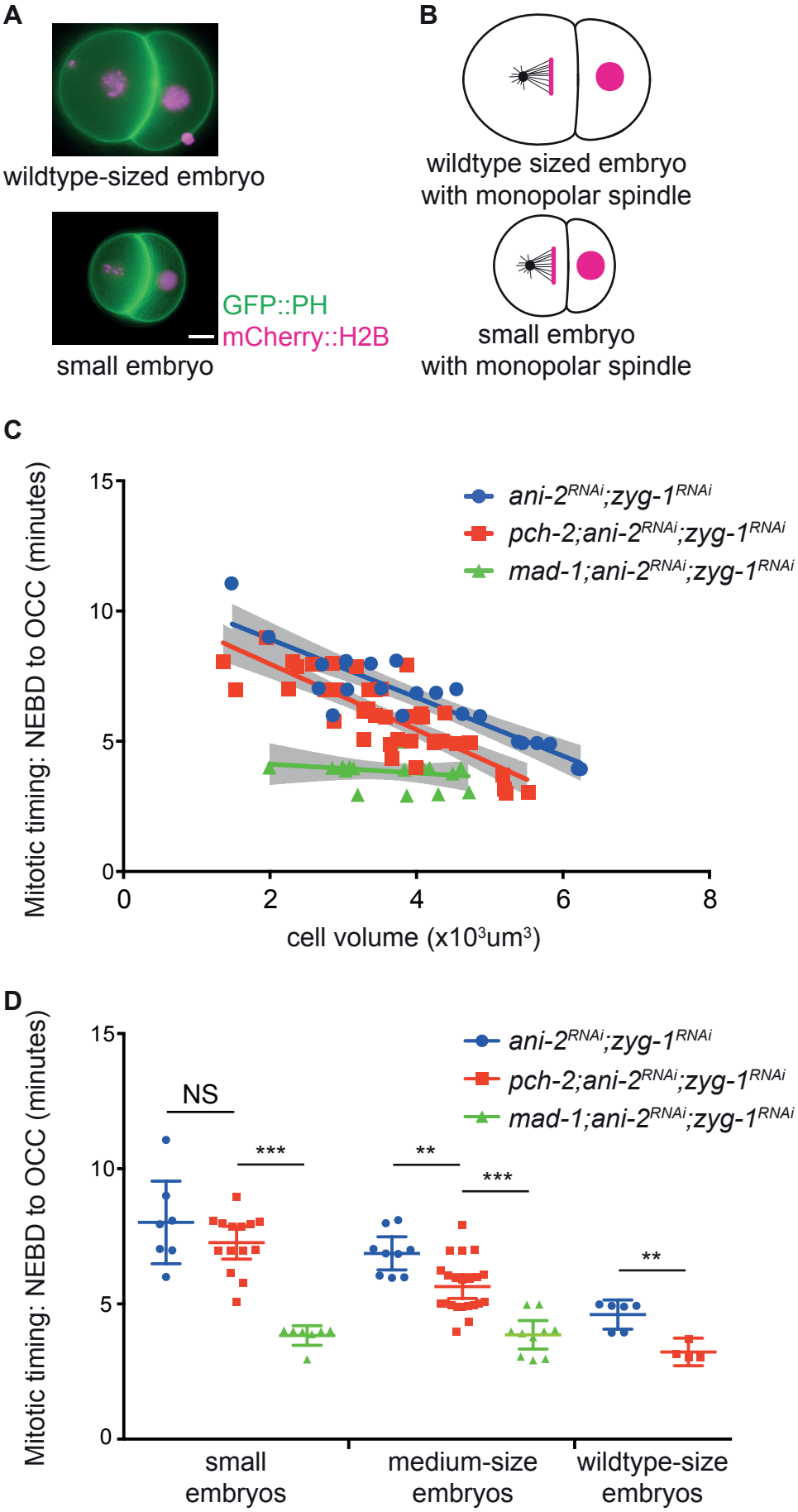
A
wildtype-sized embryo
small embryo
GFP::PH
mCherry::H2B
B
wildtype sized embryo
with monopolar spindle
small embryo
with monopolar spindle
C
Mitotic timing: NEBD to OCC (minutes)
cell volume (x10³um³)
ani-2RNAi;zyg-1RNAi
pch-2;ani-2RNAi;zyg-1RNAi
mad-1;ani-2RNAi;zyg-1RNAi
0
5
10
15
0
2
4
6
8
D
Mitotic timing: NEBD to OCC (minutes)
NS
***
**
***
**
small embryos
medium-size embryos
wildtype-size embryos

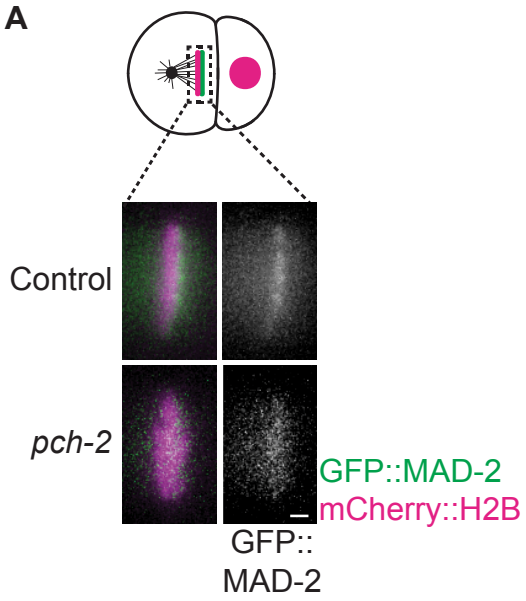
A
Control
pch-2
GFP::MAD-2
mCherry::H2B
GFP::
MAD-2

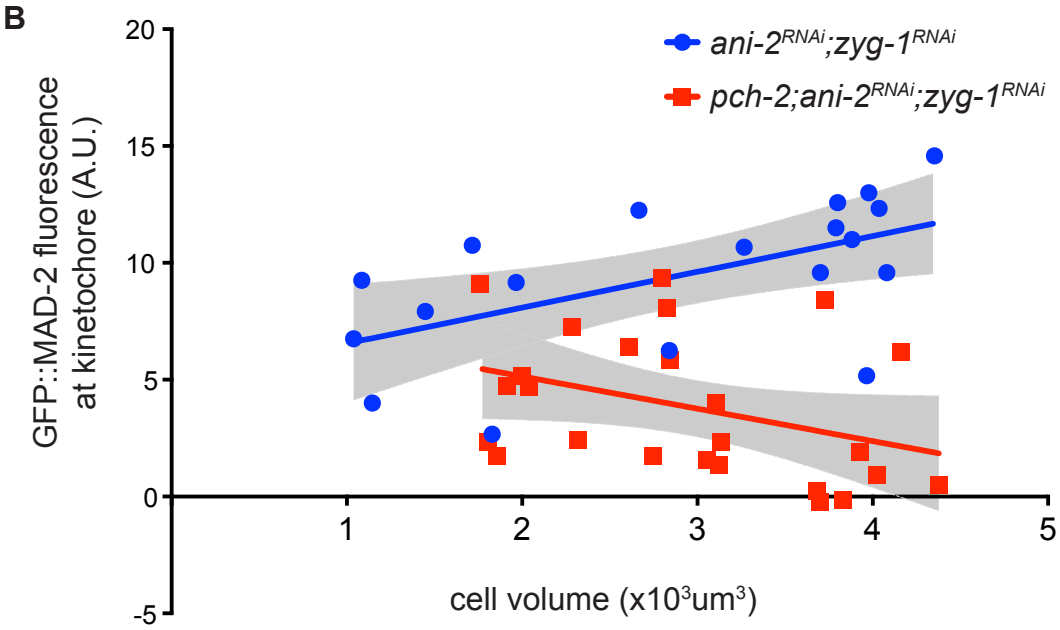
B
ani-2RNAi;zyg-1RNAi
pch-2;ani-2RNAi;zyg-1RNAi
GFP::MAD-2 fluorescence at kinetochore (A.U.)
cell volume (x10³um³)
20
15
10
5
0
-5
1
2
3
4
5

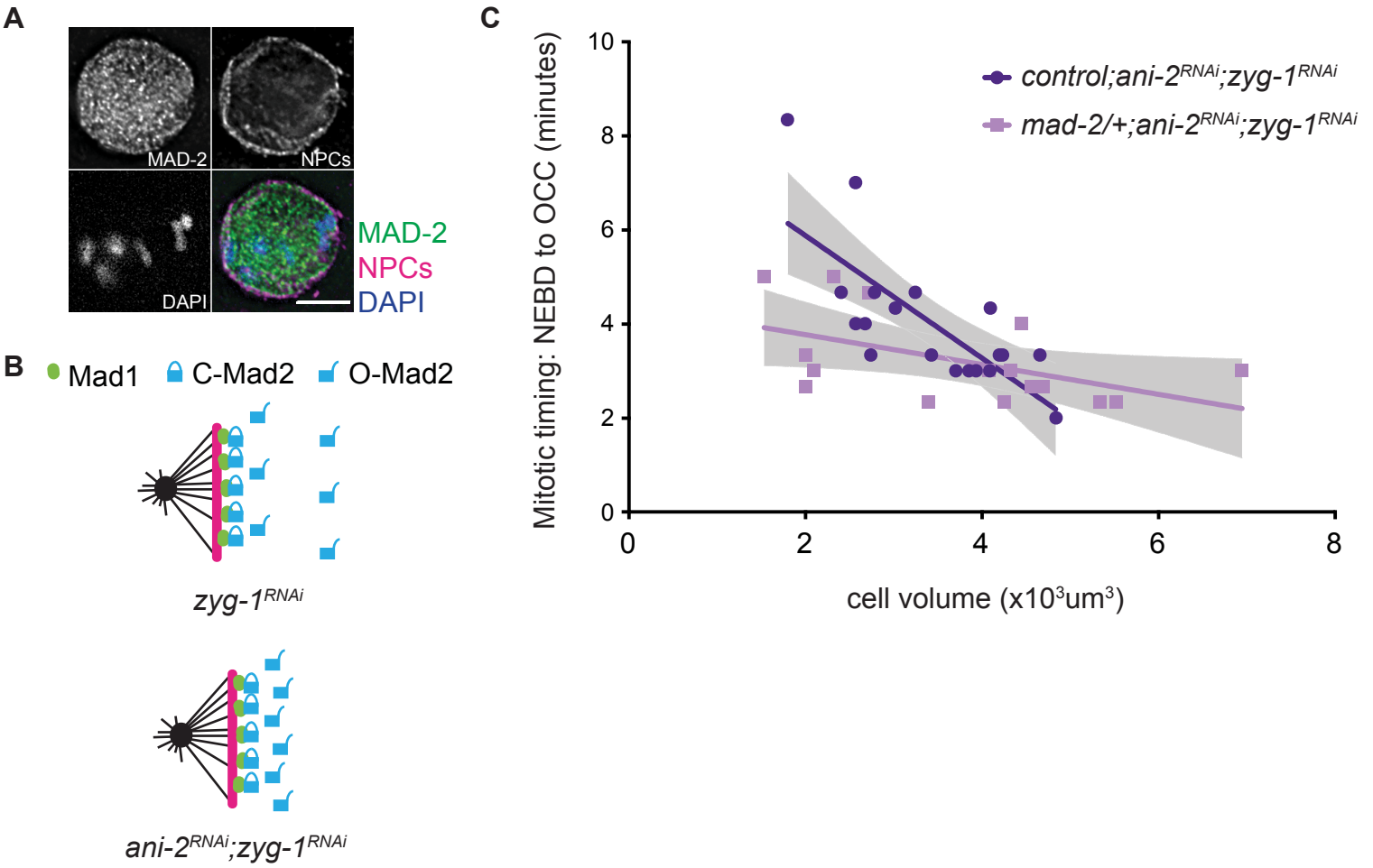
A
MAD-2
NPCs
DAPI
MAD-2
NPCs
DAPI
B
Mad1
C-Mad2
O-Mad2
zyg-1RNAi
ani-2RNAi;zyg-1RNAi
C
control;ani-2RNAi;zyg-1RNAi
mad-2/+;ani-2RNAi;zyg-1RNAi
Mitotic timing: NEBD to OCC (minutes)
cell volume (x10³um³)
0
2
4
6
8
10

Défachelles et. al., Figure 4

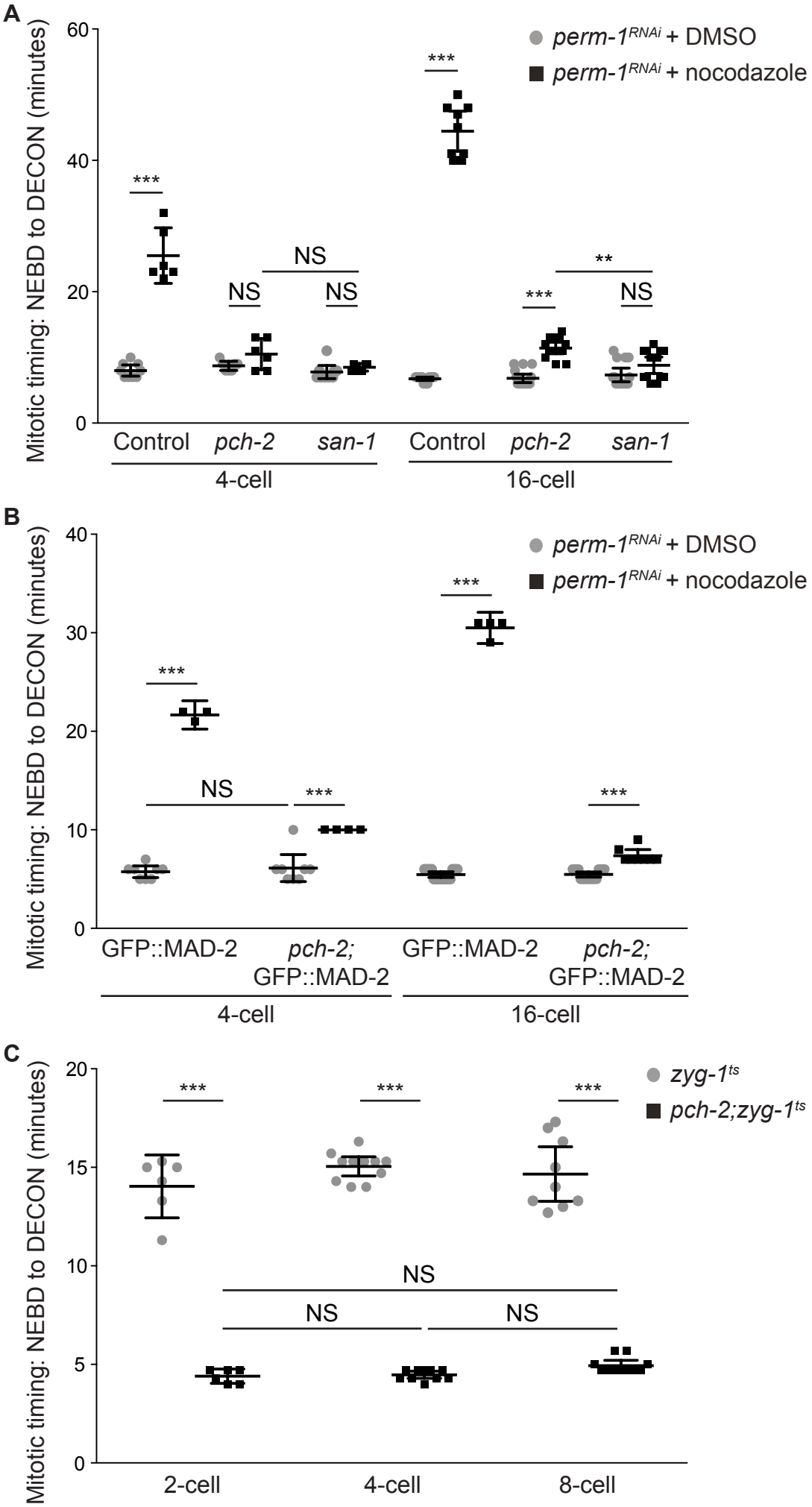

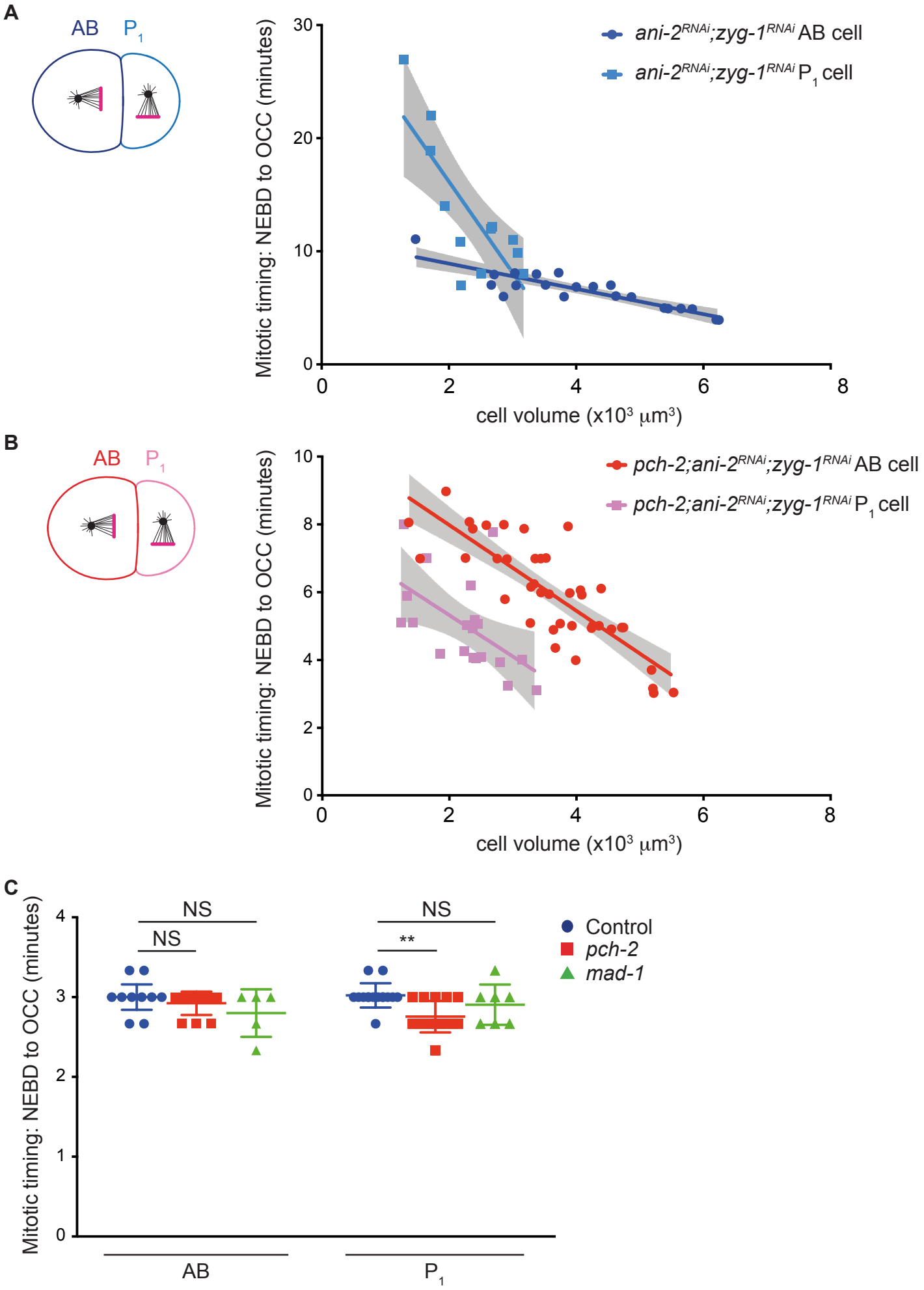
A
AB
P1
Mitotic timing: NEBD to OCC (minutes)
cell volume (x10³ µm³)
ani-2RNAi;zyg-1RNAi AB cell
ani-2RNAi;zyg-1RNAi P1 cell
B
AB
P1
Mitotic timing: NEBD to OCC (minutes)
cell volume (x10³ µm³)
pch-2;ani-2RNAi;zyg-1RNAi AB cell
pch-2;ani-2RNAi;zyg-1RNAi P1 cell
C
Mitotic timing: NEBD to OCC (minutes)
NS
NS
NS
**
Control
pch-2
mad-1
AB
P1

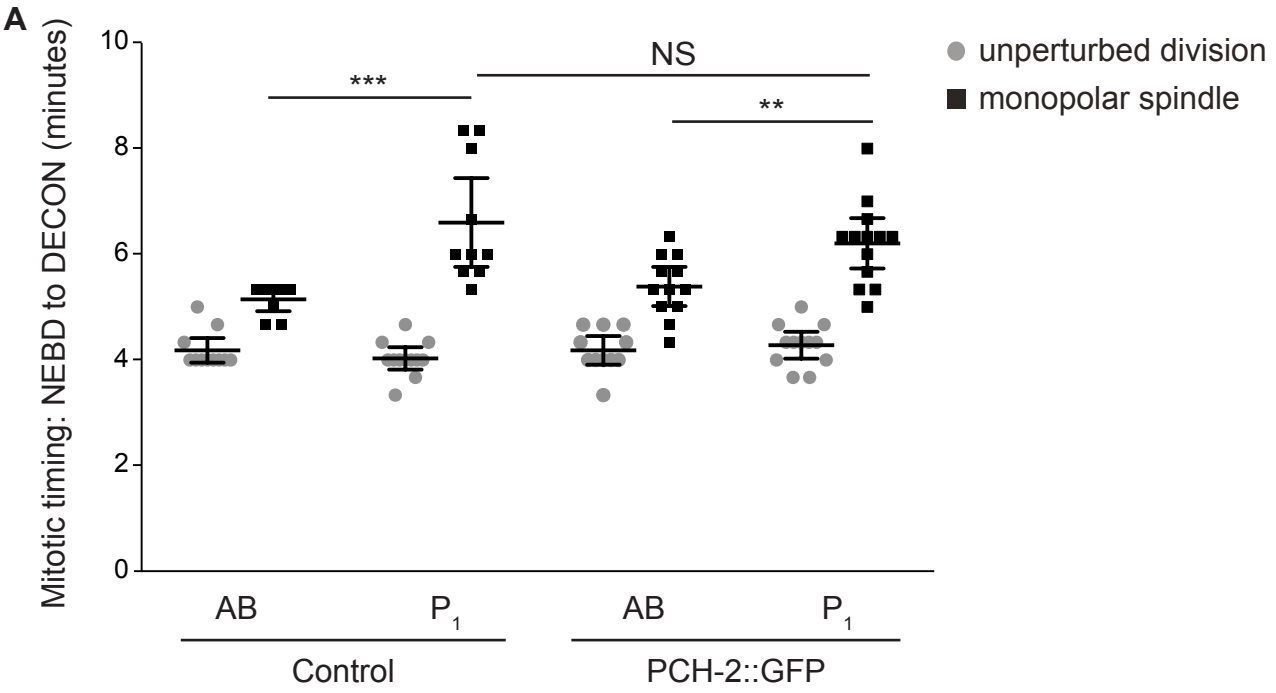
A
Mitotic timing: NEBD to DECON (minutes)
10
8
6
4
2
0
***
NS
**
unperturbed division
monopolar spindle
AB
P1
AB
P1
Control
PCH-2::GFP

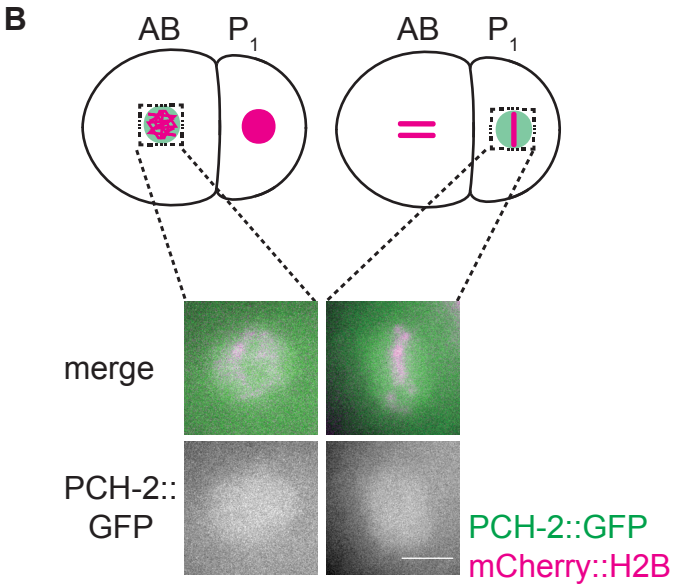
B
AB
P1
AB
P1
merge
PCH-2::
GFP
PCH-2::GFP
mCherry::H2B

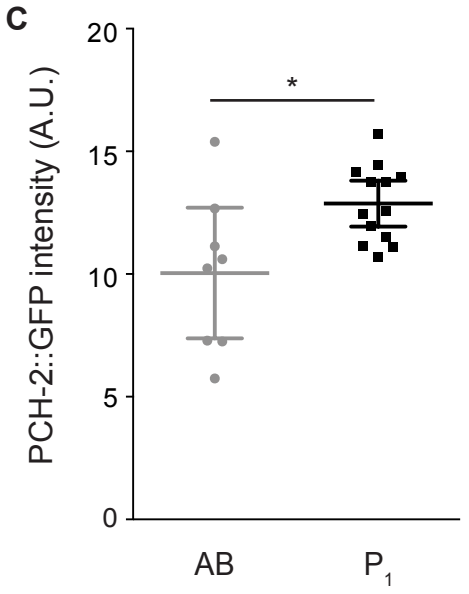
C
PCH-2::GFP intensity (A.U.)
20
15
10
5
0
*
AB
P1

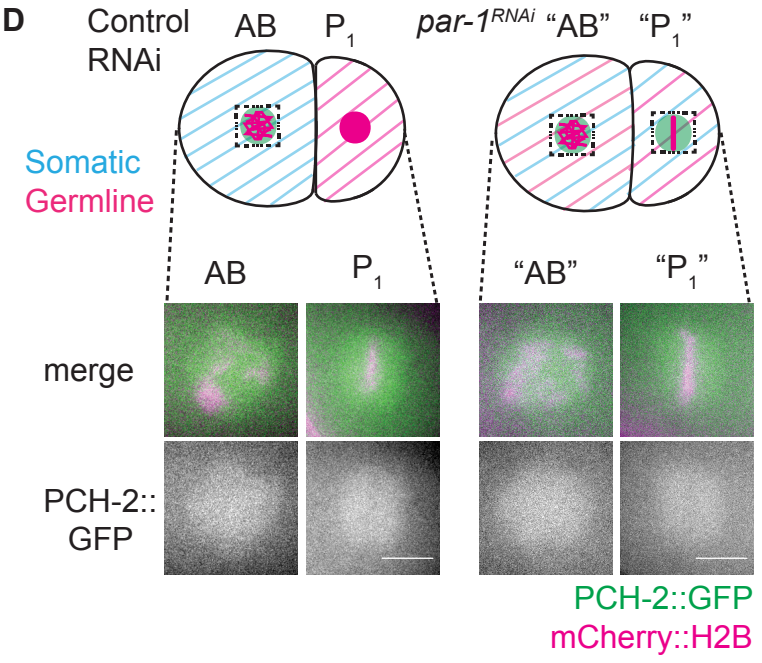
D
Control
RNAi
AB
P1
par-1RNAi
"AB"
"P1"
Somatic
Germline
AB
P1
"AB"
"P1"
merge
PCH-2::
GFP
PCH-2::GFP
mCherry::H2B

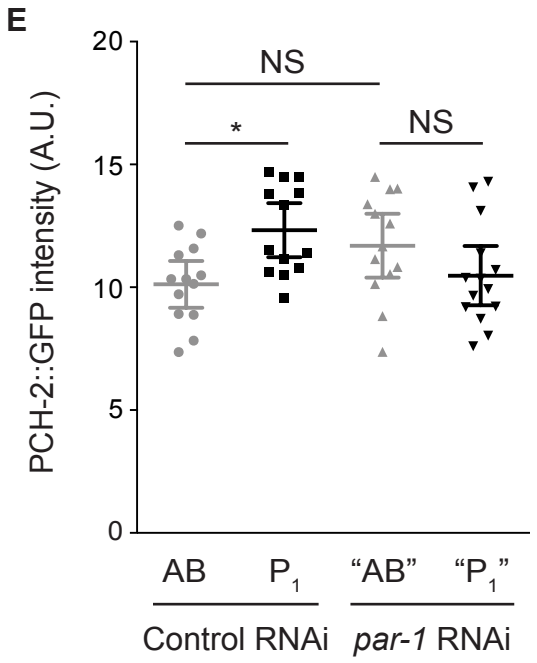
E
PCH-2::GFP intensity (A.U.)
20
15
10
5
0
NS
*
NS
AB
P1
"AB"
"P1"
Control RNAi
par-1 RNAi

Défachelles et. al., Figure 7

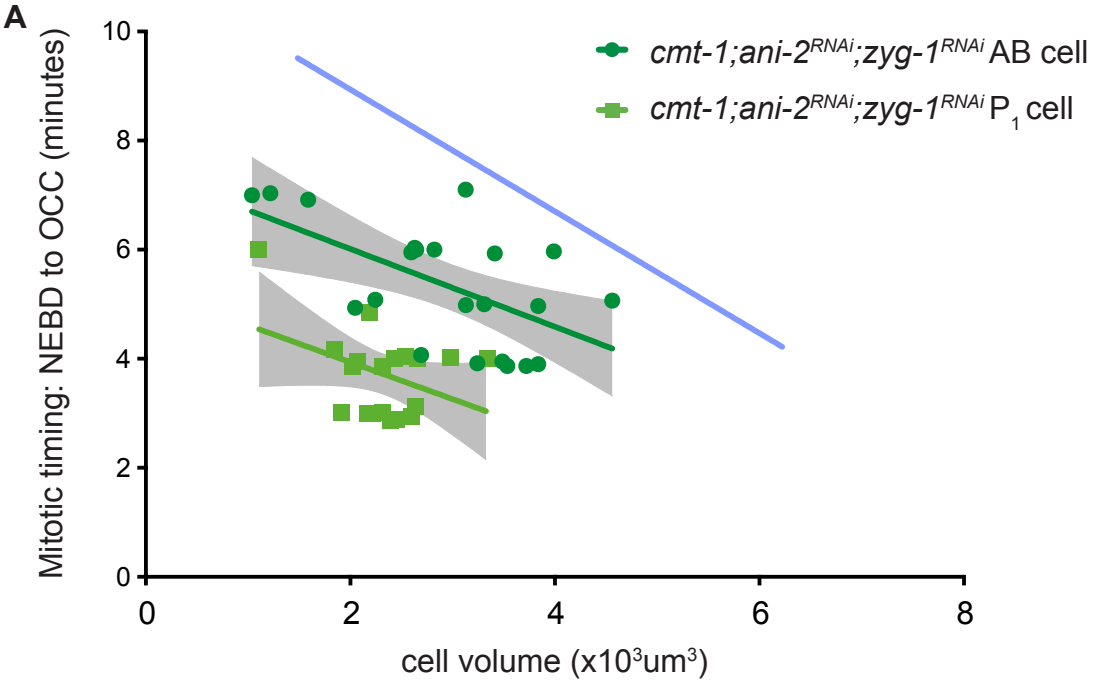

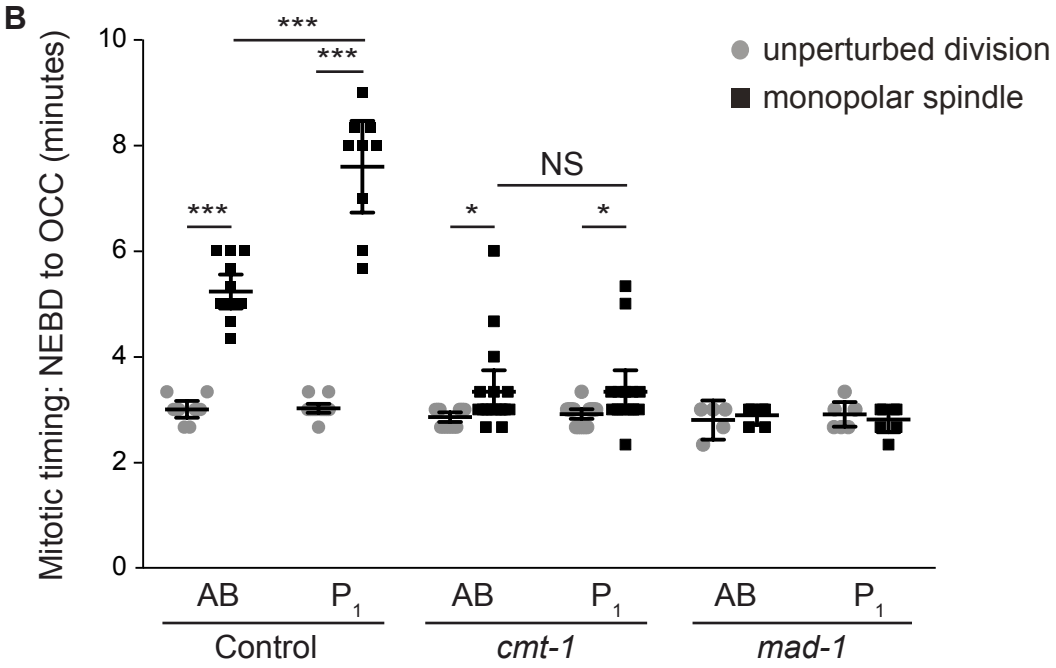

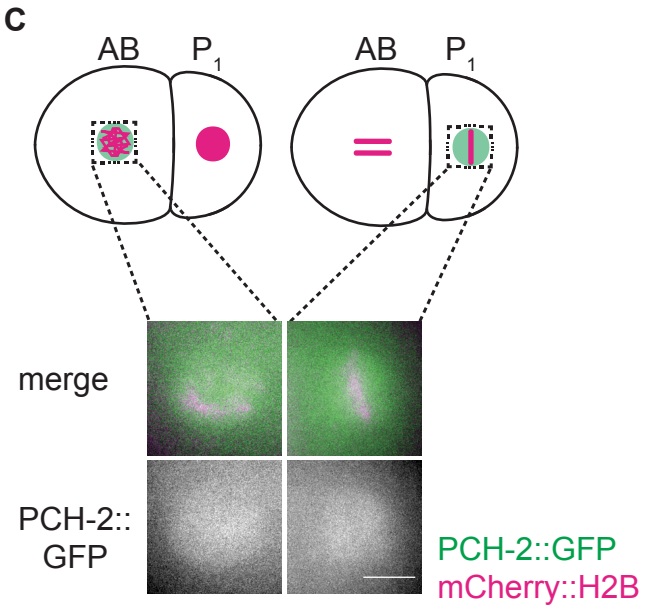

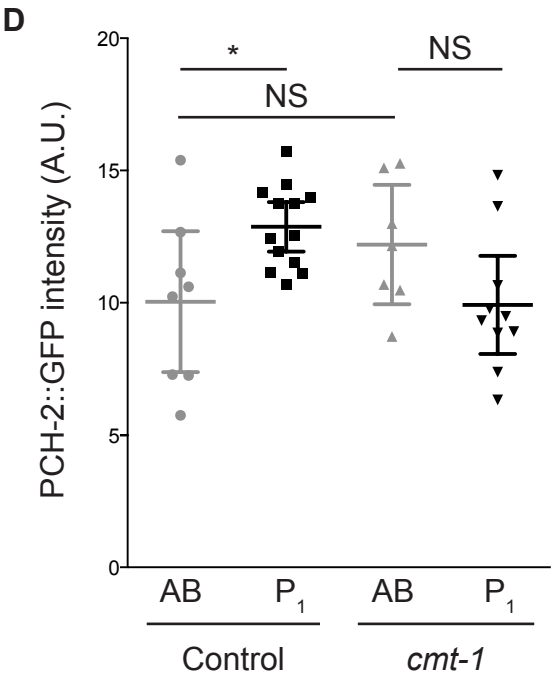

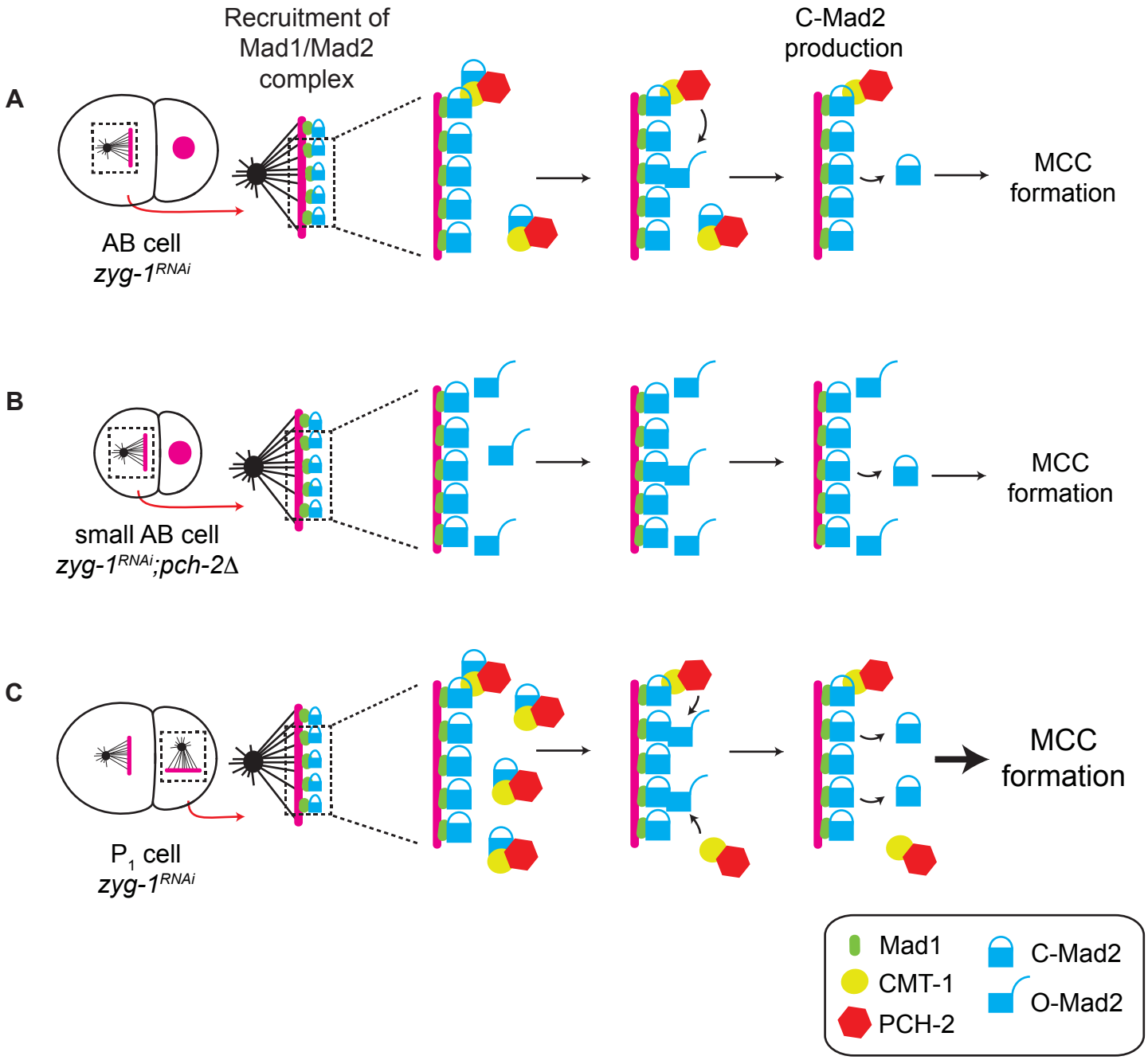
A
Recruitment of
Mad1/Mad2
complex
C-Mad2
production
AB cell
zyg-1RNAi
MCC
formation
B
small AB cell
zyg-1RNAi;pch-2Δ
MCC
formation
C
P1 cell
zyg-1RNAi
MCC
formation
Mad1
CMT-1
PCH-2
C-Mad2
O-Mad2

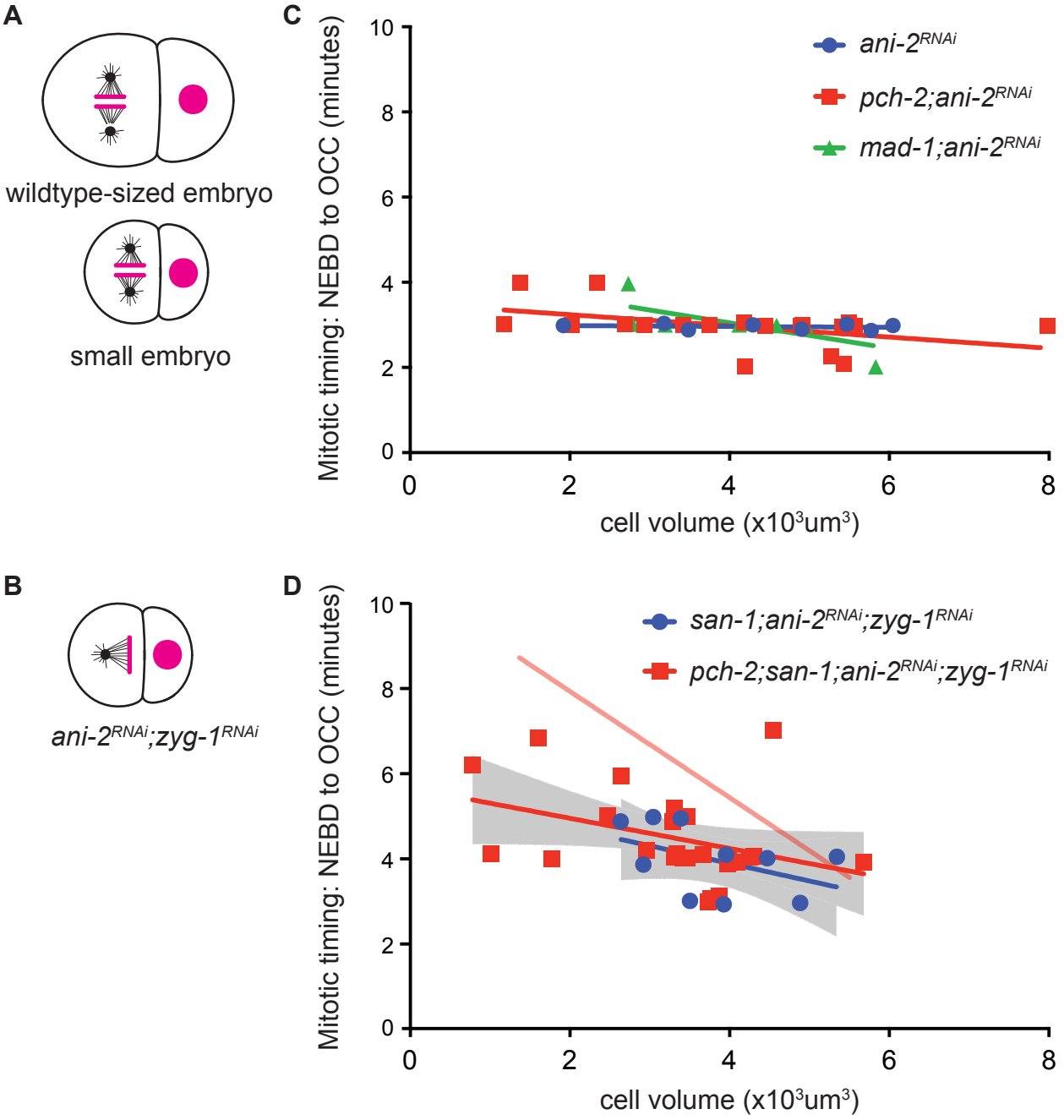
A
wildtype-sized embryo
small embryo
B
ani-2RNAi;zyg-1RNAi
C
ani-2RNAi
pch-2;ani-2RNAi
mad-1;ani-2RNAi
Mitotic timing: NEBD to OCC (minutes)
cell volume (x10³um³)
D
san-1;ani-2RNAi;zyg-1RNAi
pch-2;san-1;ani-2RNAi;zyg-1RNAi
Mitotic timing: NEBD to OCC (minutes)
cell volume (x10³um³)

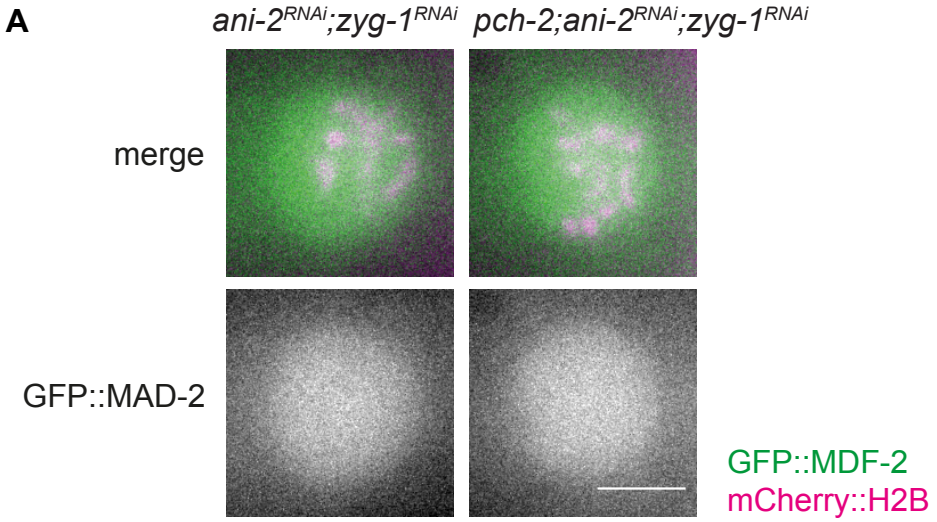
A
ani-2RNAi;zyg-1RNAi
pch-2;ani-2RNAi;zyg-1RNAi
merge
GFP::MAD-2
GFP::MDF-2
mCherry::H2B

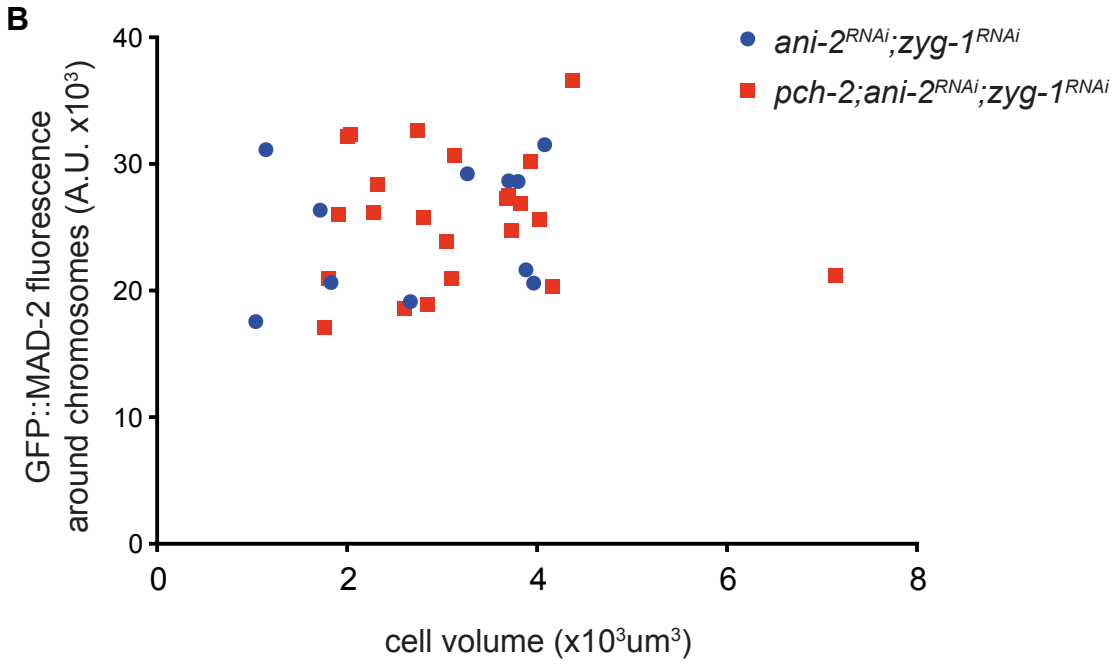
B
ani-2RNAi;zyg-1RNAi
pch-2;ani-2RNAi;zyg-1RNAi
GFP::MAD-2 fluorescence around chromosomes (A.U. x10³)
cell volume (x10³um³)
0
10
20
30
40
0
2
4
6
8

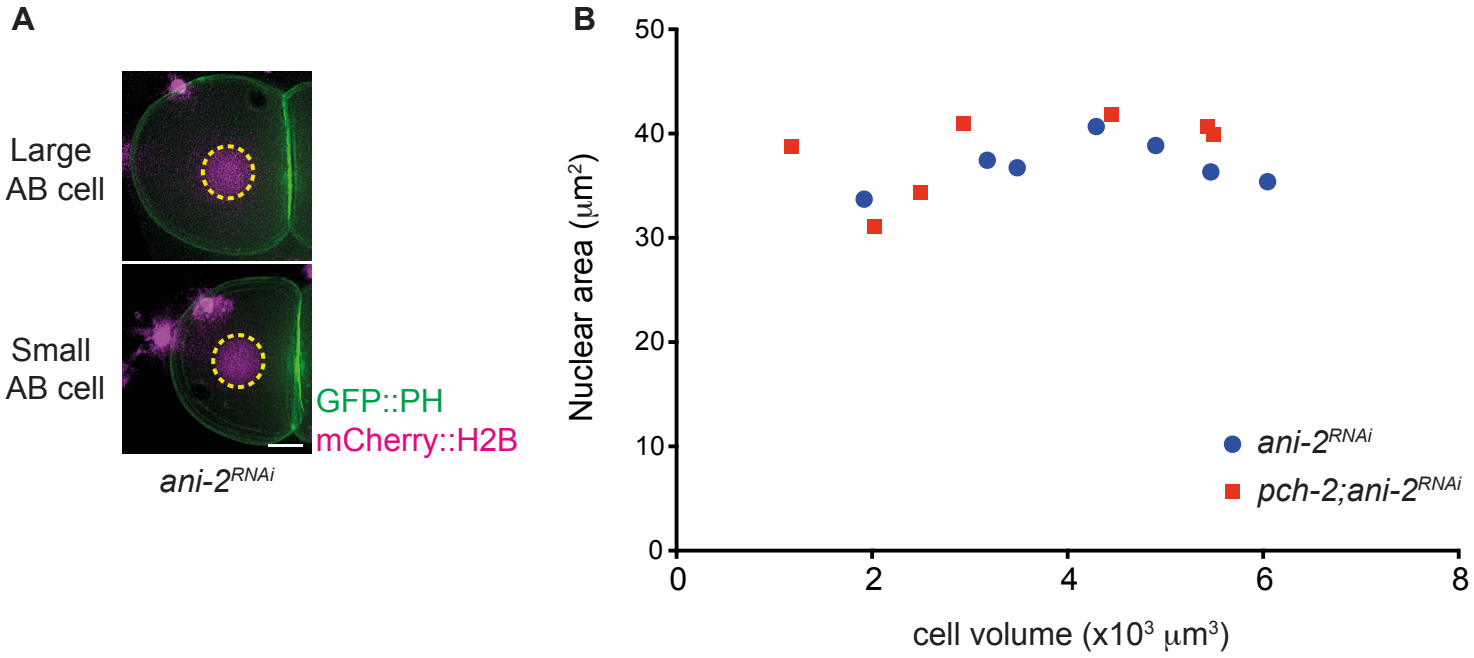
A
Large AB cell
Small AB cell
GFP::PH
mCherry::H2B
ani-2RNAi
B
Nuclear area (μm2)
cell volume (x103 μm3)
ani-2RNAi
pch-2;ani-2RNAi
0
10
20
30
40
50
0
2
4
6
8

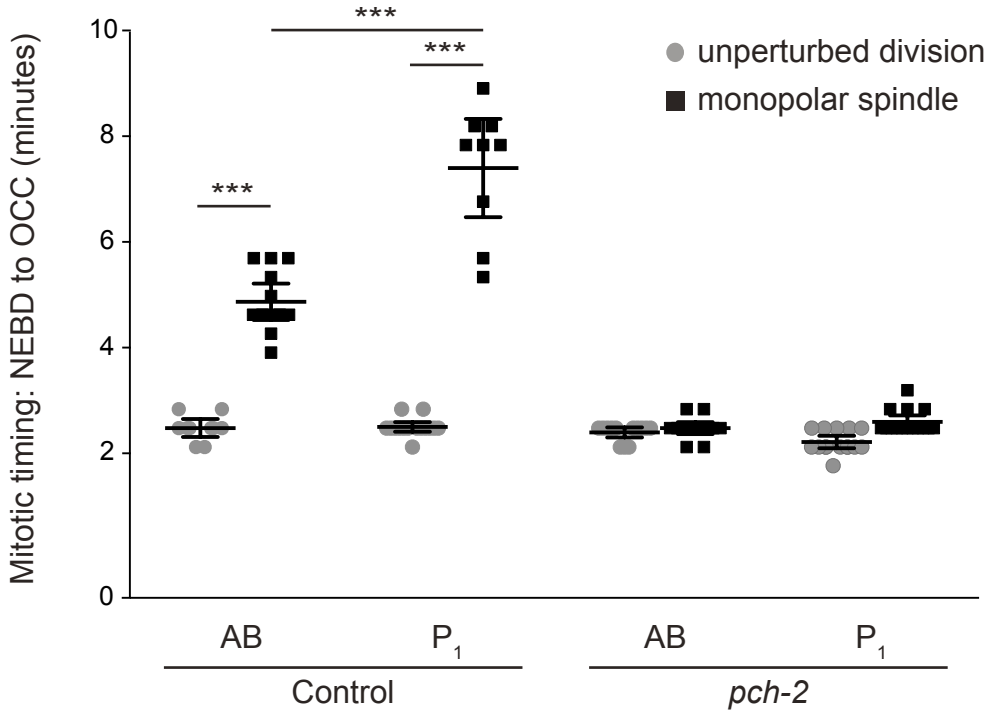
Mitotic timing: NEBD to OCC (minutes)
10
8
6
4
2
0
***
***
***
unperturbed division
monopolar spindle
AB
P1
AB
P1
Control
pch-2

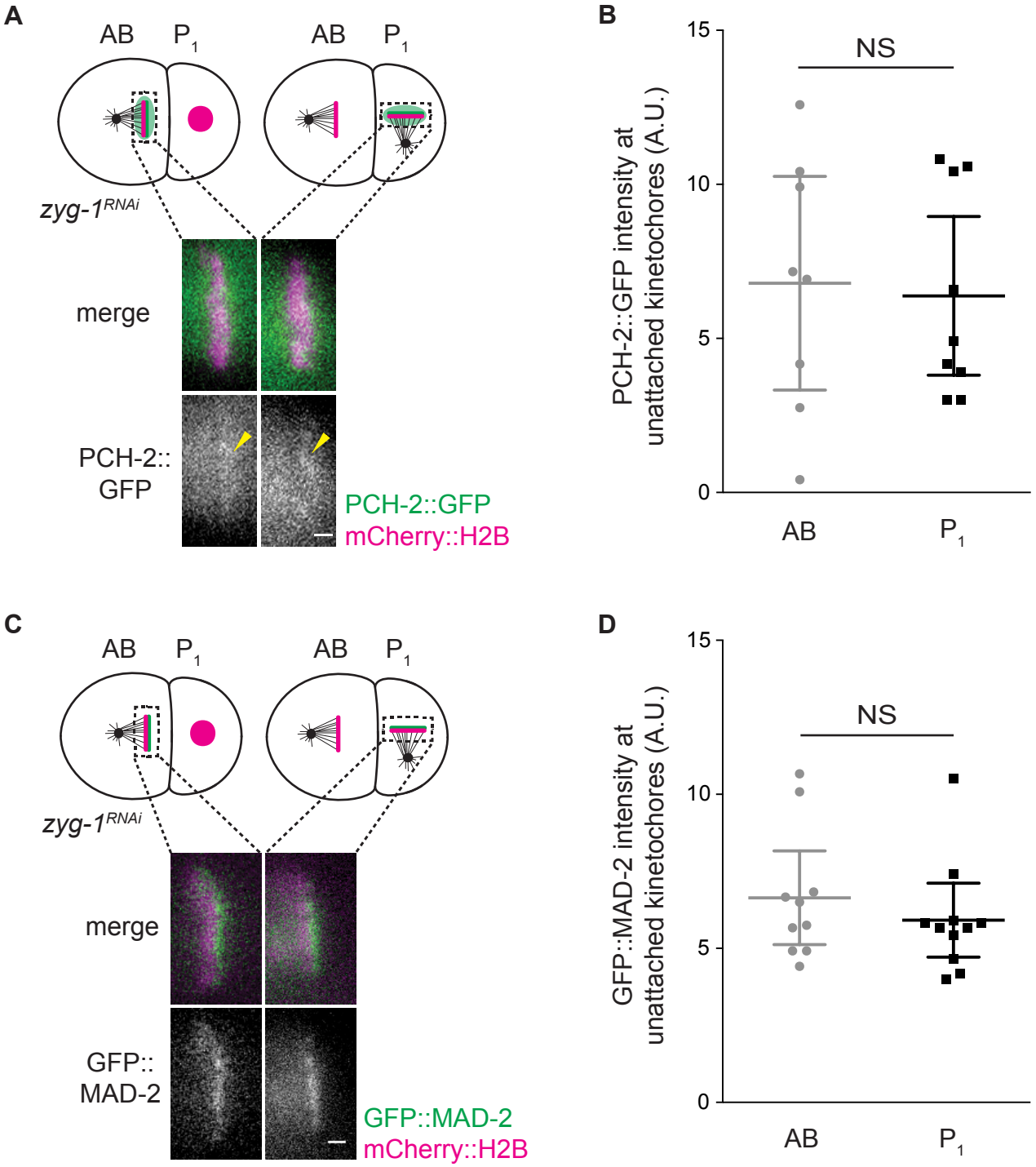
A
AB
P1
AB
P1
zyg-1RNAi
merge
PCH-2::
GFP
PCH-2::GFP
mCherry::H2B
B
NS
PCH-2::GFP intensity at
unattached kinetochores (A.U.)
15
10
5
0
AB
P1
C
AB
P1
AB
P1
zyg-1RNAi
merge
GFP::
MAD-2
GFP::MAD-2
mCherry::H2B
D
NS
GFP::MAD-2 intensity at
unattached kinetochores (A.U.)
15
10
5
0
AB
P1

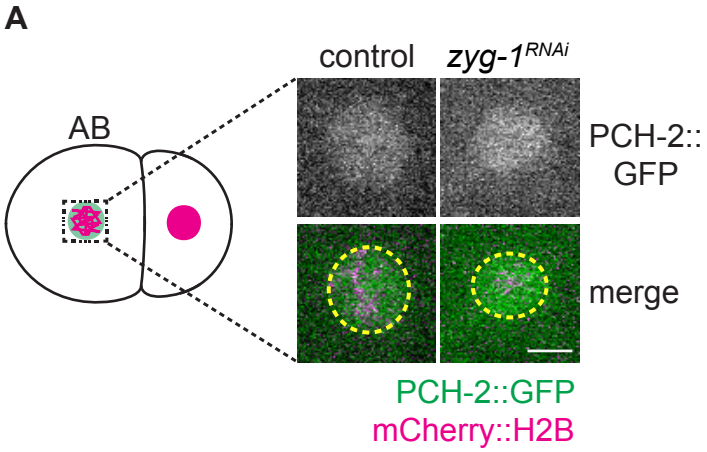
A
control
zyg-1RNAi
AB
PCH-2::
GFP
merge
PCH-2::GFP
mCherry::H2B

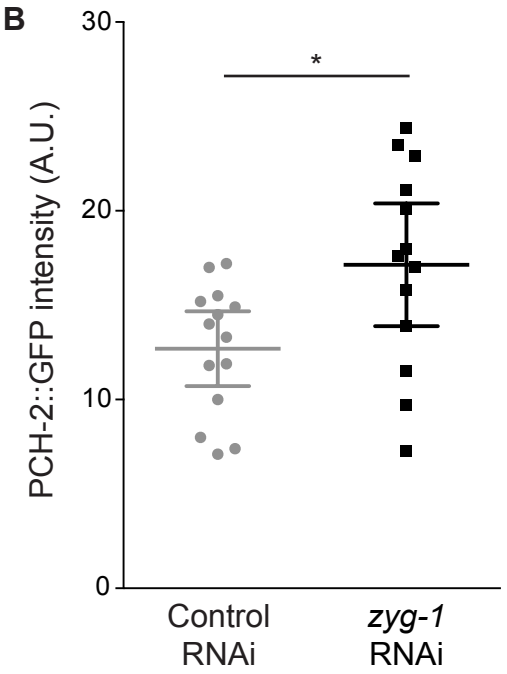
B
PCH-2::GFP intensity (A.U.)
30
20
10
0
*
Control
RNAi
zyg-1
RNAi

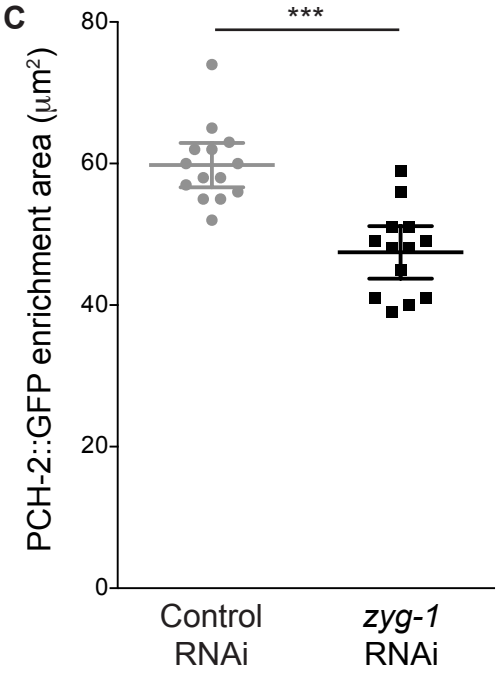
C
PCH-2::GFP enrichment area (μm2)
80
60
40
20
0
***
Control
RNAi
zyg-1
RNAi

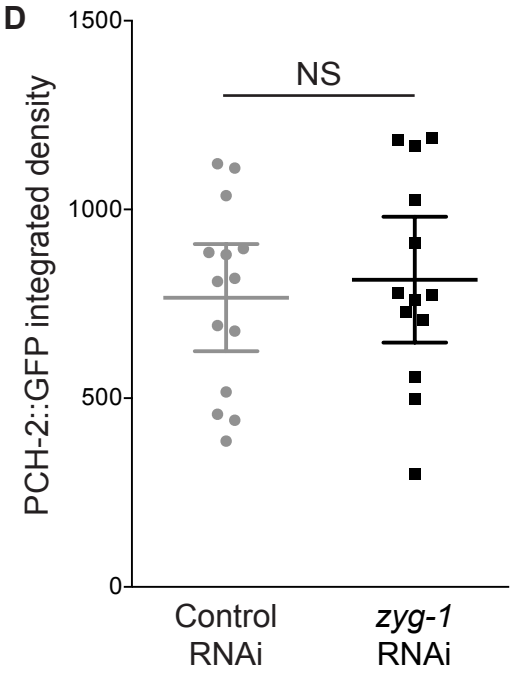
D
PCH-2::GFP integrated density
1500
1000
500
0
NS
Control
RNAi
zyg-1
RNAi

Défachelles et. al., Figure S7

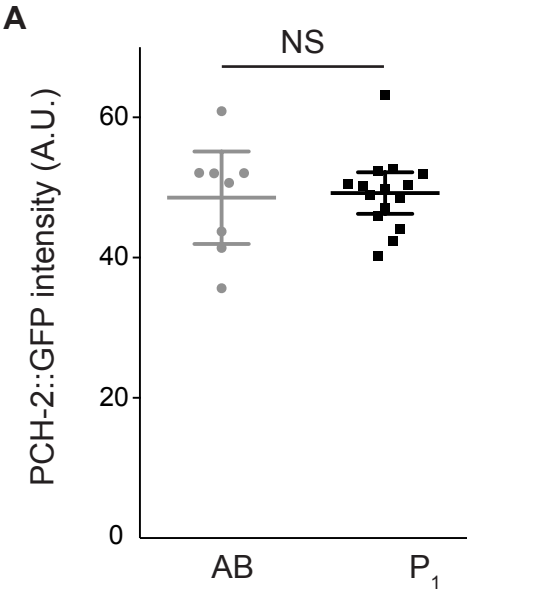

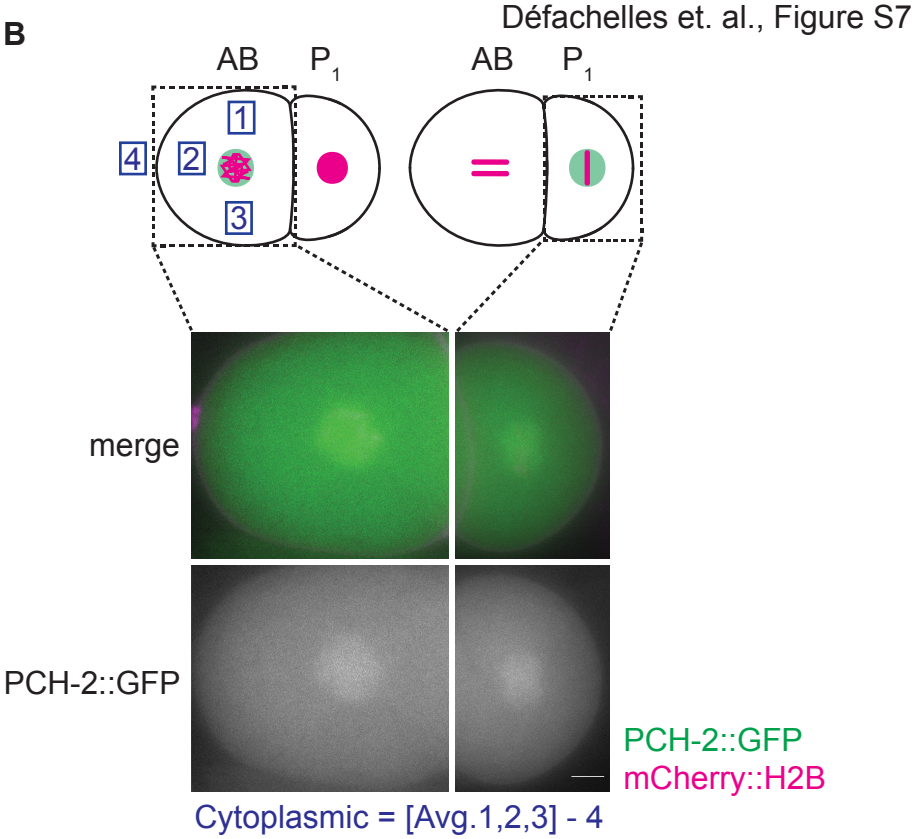

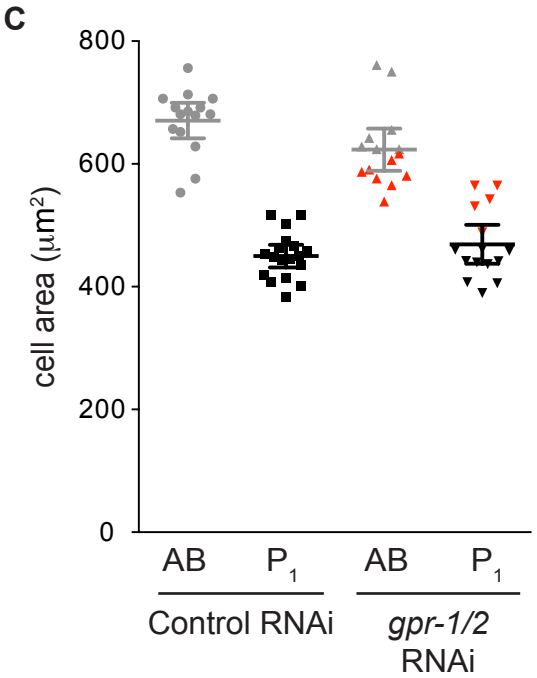

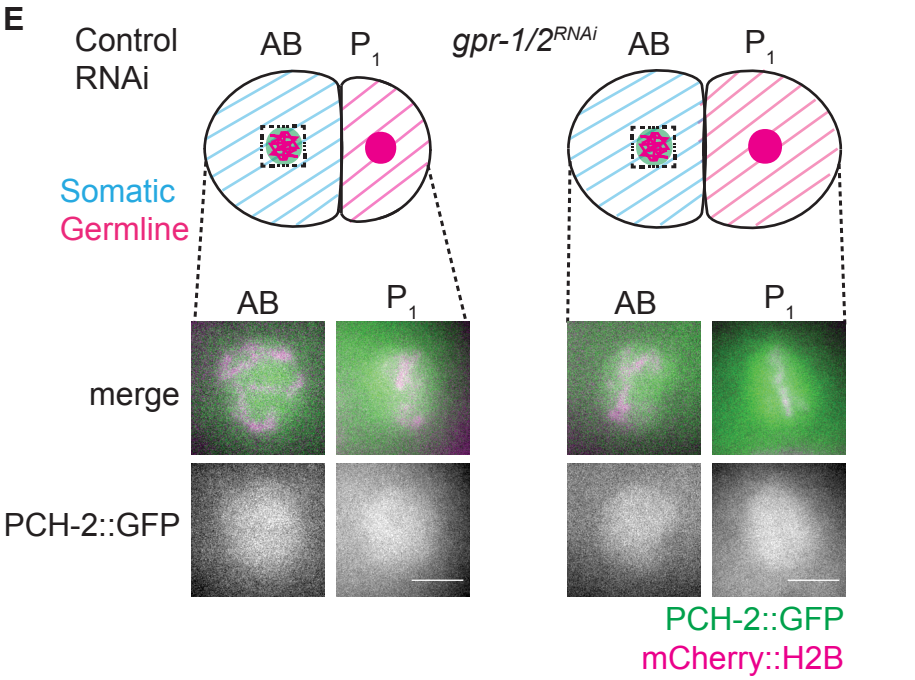

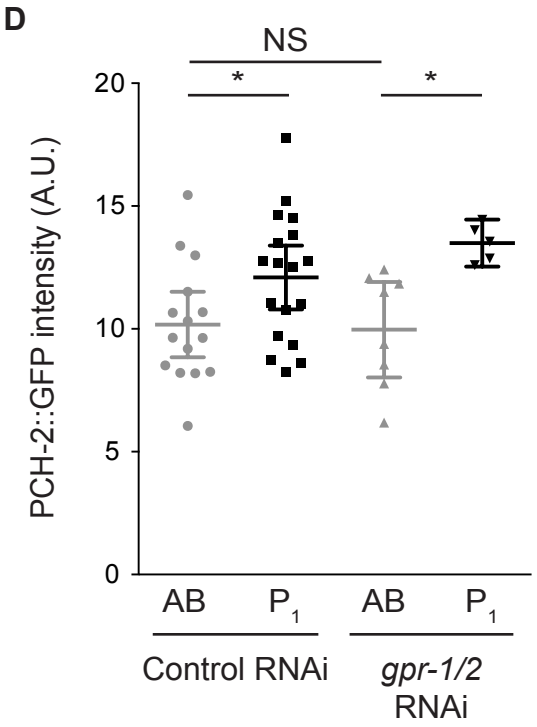

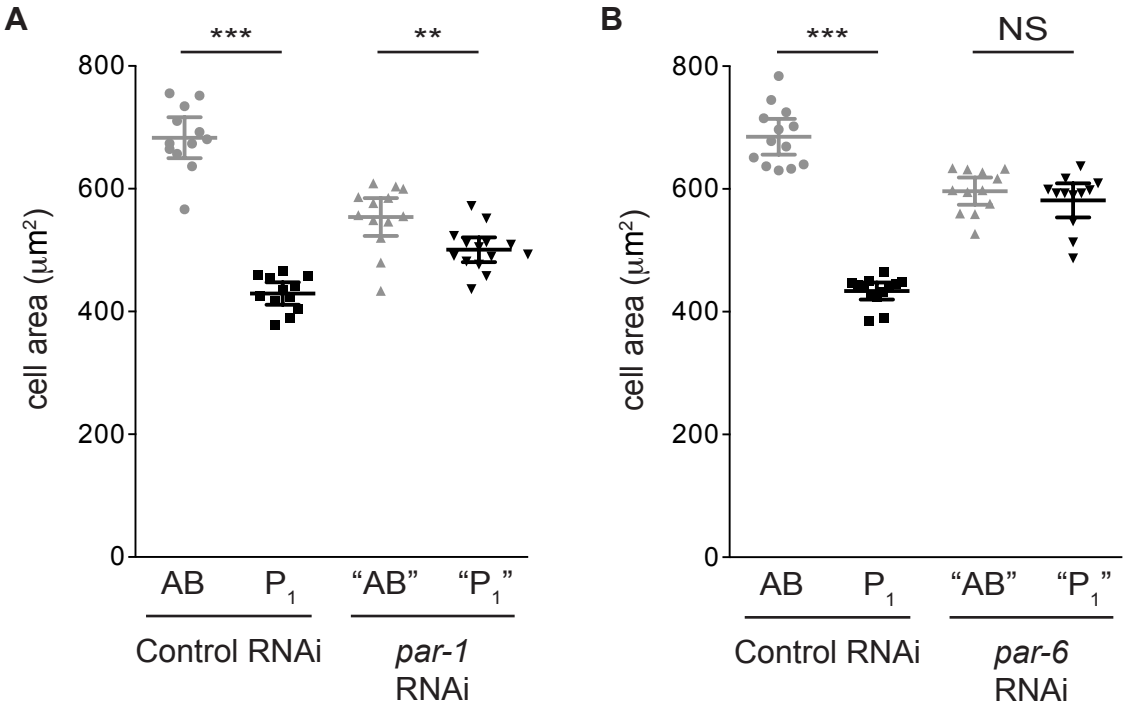
A
***
**
800
600
400
200
0
cell area (µm²)
AB
P1
"AB"
"P1"
Control RNAi
par-1 RNAi
B
***
NS
800
600
400
200
0
cell area (µm²)
AB
P1
"AB"
"P1"
Control RNAi
par-6 RNAi

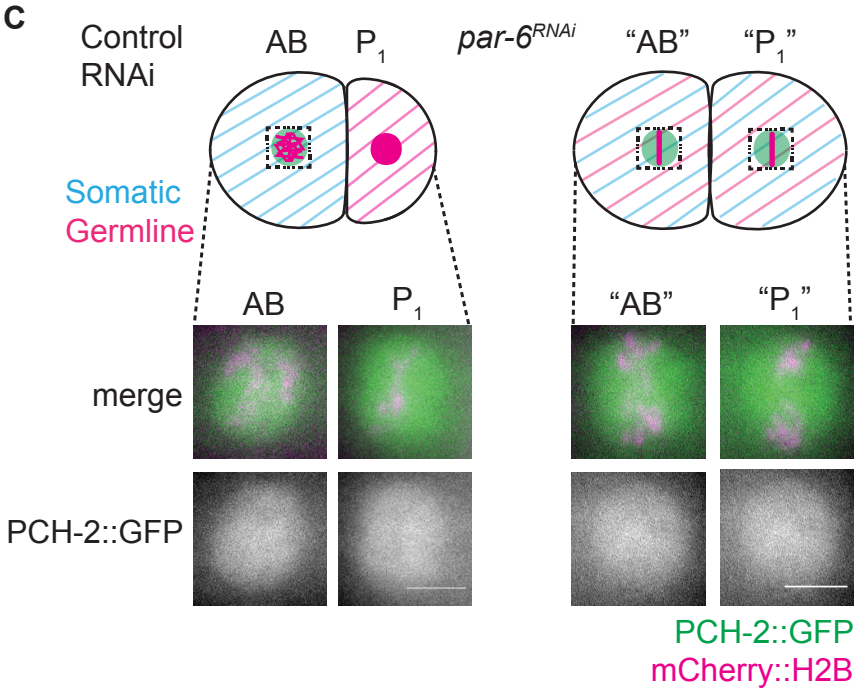
C
Control RNAi
AB
P1
par-6RNAi
"AB"
"P1"
Somatic
Germline
AB
P1
"AB"
"P1"
merge
PCH-2::GFP
PCH-2::GFP
mCherry::H2B

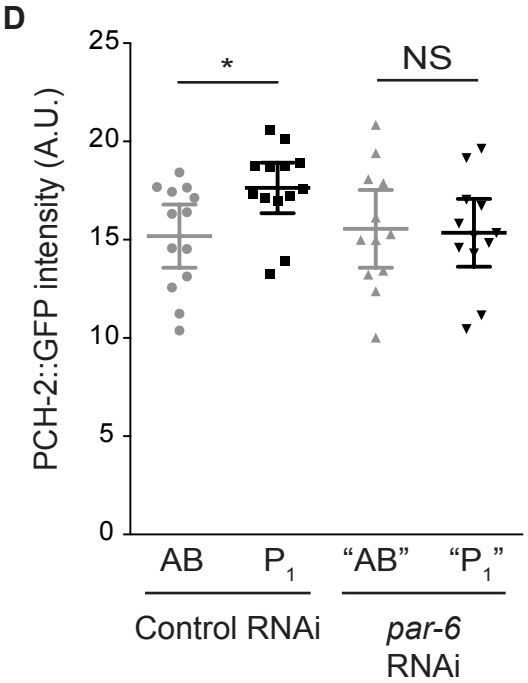
D
25
20
15
10
5
0
PCH-2::GFP intensity (A.U.)
*
NS
AB
P1
"AB"
"P1"
Control RNAi
par-6 RNAi

Table S1: Strains used in this study

Strain	Genotype
OD56	*unc-119(ed3) III; ltIs37 [pAA64; Ppie-1::mCherry::his-58; unc-119 (+)] IV*
OD95	*unc-119(ed3) III; ltIs37 [pAA64; Ppie-1::mCherry::his-58; unc-119 (+)] IV; ltIs38 [pAA1; Ppie-1::GFP::PH(PLC1delta1); unc-119(+)]*
BHL575	*pch-2(tm1458) II; unc-119(ed3) III; ltIs37 [pAA64; Ppie-1::mCherry::his-58; unc-119 (+)] IV; ltIs38 [pAA1;Ppie-1::GFP::PH(PLC1delta1); unc-119(+)]*
BHL596	*unc-119(ed3) III; ltIs37 [pAA64; Ppie-1::mCherry::his-58; unc-119 (+)] IV; ltIs38 [pAA1; Ppie-1::GFP::PH(PLC1delta1); unc-119(+)]; mdf-1(av19) V*
BHL600	*unc-119(ed3) III; ltIs37 [pAA64; Ppie-1::mCherry::his-58; unc-119 (+)] IV; ltIs52 [pOD379; Ppie-1::GFP::MDF-2; unc-119 (+)]*
BHL604	*pch-2(tm1458) II; unc-119(ed3) III; ltIs37 [pAA64; Ppie-1::mCherry::his-58; unc-119 (+)] IV; ltIs52 [pOD379; Ppie-1::GFP::MDF-2; unc-119 (+)]*
BHL608	*cmt-1(ok2879) I; unc-119(ed3) III; ltIs37 [pAA64; Ppie-1::mCherry::his-58; unc-119 (+)] IV; ltIs38 [pAA1;Ppie-1::GFP::PH(PLC1delta1); unc-119(+)]*
BHL664	*Ppch-2::pch-2::GFP-3XFLAG (blt4 [pCN94]) II; unc-119(ed3) III; ltIs37 [pAA64; Ppie-1::mCherry::his-58; unc-119 (+)] IV*
BHL666	*unc-119(ed3) III; ltIs37 [pAA64; Ppie-1::mCherry::his-58; unc-119 (+)];mdf-2(tm2190) IV/nT1[qIs51](IV;V) ltIs38 [pAA1; Ppie-1::GFP::PH(PLC1delta1); unc-119(+)]*
BHL883	*san-1/mdf-3 (ok1580) I; pch-2(tm1458) II; unc-119(ed3) III; ltIs37 [pAA64; Ppie-1::mCherry::his-58; unc-119 (+)] IV; ltIs38 [pAA1; Ppie-1::GFP::PH(PLC1delta1); unc-119(+)]*
BHL887	*cmt-1(ok2879) I; pch-2::GFP-3XFLAG (blt4 [pCN94]) II; unc-119(ed3) III; ltIs44[pAA173; pPie-1::mCherry::PH(PLC1delta1); unc-119(+)]; ltIs37 [pAA64; Ppie-1::mCherry::his-58; unc-119 (+)] IV*
BHL888	*unc-119(ed3) III; ltIs44 [pAA173; pPie-1::mCherry::PH(PLC1delta1); unc-119(+)]; ltIs52 [pOD379; Ppie-1::GFP::mdf-2; unc-119 (+)]; ltIs37 [pAA64; Ppie-1::mCherry::his-58; unc-119 (+)] IV*
BHL889	*pch-2(tm1458) II; unc-119(ed3) III; ltIs44 [pAA173; pPie-1::mCherry::PH(PLC1delta1); unc-119(+)]; ltIs52 [pOD379; Ppie-1::GFP::mdf-2; unc-119 (+)]; ltIs37 [pAA64; Ppie-1::mCherry::his-58; unc-119 (+)] IV*
BHL891	*unc-119(ed3) III; ltIs37 [pAA64; Ppie-1::mCherry::his-58; unc-119 (+)] IV; ltIs24[pAZ132; pPie-1::GFP::tba-2; unc-119(+)]*
BHL892	*pch-2 (tm1458) II; unc-119(ed3) III; ltIs37 [pAA64; Ppie-1::mCherry::his-58; unc-119 (+)] IV; ltIs24 [pAZ132; pPie-1::GFP::tba-2; unc-119(+)]*
BHL893	*san-1/mdf-3 (ok1580) I; unc-119(ed3) III; ltIs37 [pAA64; Ppie-1::mCherry::his-58; unc-119 (+)] IV; ltIs38 [pAA1; Ppie-1::GFP::PH(PLC1delta1); unc-119(+)]*
BHL904	*Ppch-2::pch-2::GFP-3XFLAG (blt4 [pCN94]) II; unc-119(ed3) III; ltIs44[pAA173; pPie-1::mCherry::PH(PLC1delta1); unc-119(+)]; ltIs37 [pAA64; Ppie-1::mCherry::his-58; unc-119 (+)] IV*
BHL950	*pch-2(tm1458) II; unc-119(ed3) III; ltIs37 [pAA64; Ppie-1::mCherry::his-58; unc-119 (+)]; mdf-2(tm2190) IV/nT1[qIs51](IV;V); ltIs38 [pAA1; Ppie-1::GFP::PH(PLC1delta1); unc-119(+)]*

BHL958	*unc-119(ed3) III; ltIs37 [pAA64; Ppie-1::mCherry::his-58; unc-119 (+)] IV/nT1[qIs51](IV;V); ltIs38 [pAA1; Ppie-1::GFP::PH(PLC1delta1); unc-119(+)]*
BHL964	*zyg-1(or297) unc-4(e120) II unc-119(ed3) III; ltIs37 [pAA64; Ppie-1::mCherry::his-58; unc-119 (+)] IV; ltIs24[pAZ132; pPie-1::GFP::tba-2; unc-119(+)]*
BHL965	*zyg-1(or297) pch-2(tm1458) unc-4(e120) II; unc-119(ed3) III; ltIs37 [pAA64; Ppie-1::mCherry::his-58; unc-119 (+)] IV; ltIs24[pAZ132; pPie-1::GFP::tba-2; unc-119(+)]*
GAL5	*san-1/mdf-3 (mat5) I; unc-119(ed3) III; ruIs57[Ppie-1::GFP::tubulin + unc-119(+)]; ltIs37[pie-1p::mCherry::his-58 (pAA64) + unc-119(+)] IV*